Department of Physics and Astronomy
University of Heidelberg

Bachelor Thesis in Physics
submitted by

Mathias Neidig

born in Bad Friedrichshall (Germany)

2010

A Frequency Stabilised Diode Laser for Exploring the Properties of a Lithium MOT

This Bachelor Thesis has been carried out by Mathias Neidig at the
Kirchhoff-Institut für Physik
under the supervision of
Prof. Dr. M.K. Oberthaler

Abstract

This bachelor thesis describes the setup of a lithium lasersystem for an experiment with fermionic lithium and bosonic sodium and the cooling of lithium atoms with a Zeeman slower as well as the trapping with a magneto-optical trap.
The theory part in the beginning summarizes the basic features of the atomic structure of alkali atoms.
Subsequently, the experimental implementation of a frequency stabilized diode laser for lithium, which has a stability of approximately 1 MHz, is shown.
The basics of laser cooling using a Zeeman slower are explained and for our case with lithium specified. Besides, a commonly used method to probe atom clouds, the absorption imaging method, is explained.
Finally, our experimental results are shown, in which we optimise the size of our trapped atom cloud with the parameters the slower provides us with. In addition, our total atom number is determined by capturing the fluorescence on a photodiode and via absorption imaging, whereas the latter one is presented in detail in this thesis.

Kurzfassung

Diese Bachelor-Arbeit beschreibt den Aufbau eines Lithium Lasersystems für ein Experiment mit fermionischen Lithium und bosonischem Natrium und das Kühlen von Lithium Atomen mit einem Zeeman-Abbremser sowie das Fangen der gekühlten Atome in einer magneto-optischen Falle.
Im anfänglichen Theorieteil werden kurz die theoretischen Grundlagen der Atomstruktur von Alkali-Atomen aufgeführt.
Anschließend wird die experimentelle Umsetzung unseres frequenzstabilisierten Diodenlasers für Lithium, mit dem eine Stabilität von ungefähr 1 MHz möglich ist, dargelegt.
Die Grundlagen der Laserkühlung mit einem Zeeman-Abbremser werden erklärt und für unseren Fall mit Lithium spezifiziert. Des Weiteren wird eine weit verbreitete Methode zur quantitativen Messung von Atomwolken, die Absorptionsabbildung-Methode vorgestellt.
Als letztes werden unsere experimentellen Ergebnisse gezeigt, bei der wir die Größe der gefangenen Atomwolke mit Hilfe der Einstellungen unseres Zeeman-Abbremsers optimieren. Die Atomzahl der Wolke wird dann sowohl durch das Auffangen der Fluoreszenz auf einer Photodiode als auch durch die Absorptionsabbildungsmethode ermittelt, wobei letztere in dieser Arbeit detailliert beschrieben wird.

Contents

Contents

II

1. Introduction

The postulation of quantum mechanics by *N. Bohr* and *W. Heisenberg* at the beginning of the twentieth century changed the understanding of the atomic structure dramatically. Until then, the classical atom model of Bohr, developed in 1913, depicted the atom consisting of a nucleus with orbiting electrons at quantized radii. Though this model could explain emission and absortion spectra, being a classical description it could not explain the stability of the electrons on their orbits. When applying quantum mechanics to the hydrogen atom, one got both results, including the quantisation of the angular momenta which had been only postulated by Bohr in his model. But in 1922, *O. Stern* and *W. Gerlach* had already measured the deflection of silver atoms in an inhomogeneous magnetic field [1] and found out that it could not be explained by the angular momentum of the electrons alone. The explanation was given by *S. A. Goudsmit* and *G. E. Uhlenbeck*, introducing the so-called electron spin, an intrinsic angular momentum attributed to the electrons. The first mathematical description was given by *W. Pauli* in 1927 and one year later *P. Dirac* could show that the electron spin resulted inevitably when introducing relativistic quantum mechanics [2, 3]. In atomic spectra, this electron spin expresses itself as an additional energy splitting of the spectral lines and is known as the Fine structure.

The invention of the first laser by *T. Maiman* [4] in the sixties in combination with new spectroscopy methods, like doppler-free spectroscopy, made it possible to resolve atomic spectra even with higher precision and an additional splitting of the spectral lines could be observed. This feature was explained in essence by also attributing a spin to the nucleus and is known as the Hyperfine structure.

Thus with this knowledge of the atomic structure and the access to narrowband laser sources, one is able to manipulate the electronic states of an atomic ensemble or single atoms in a controlled way and can thus prepare for example atomic gases in specific states.

One research field emerging from these new possibilities are experiments with ultracold atomic gases. When reducing the temperature of an ultracold atomic gas, the statistical nature of the particles comes into play: All particles are divided into two elementary classes, the bosons with integer spin and the fermions with half-integer spin. Bosons obey the Bose-Einstein statistics and tend to appear in bunches whereas fermions obey the Fermi-Dirac statistic and can never occupy the same quantum state, which is known as the Pauli exclusion principle. At high temperatures, a gas consisting either of bosons or fermions can be described by the classical Maxwell-Boltzmann distribution in both cases, but beneath a critical temperature T_C, which highly depends on the system, their different statistics come into play. Already in 1924-25, *S. N. Bose* [5] and *A. Einstein* [6] predicted that bosons undergo a phase transition below T_C and that a macroscopic amount of the

bosons then occupies the lowest quantum state. This phase transition is known as Bose-Einstein condensation (BEC) and is for example a requirement for superfluidity in ^{4}Helium at temperatures below a few Kelvin. Fermions however show a complete different behaviour. For temperatures beneath the so-called Fermi temperature T_F, they become degenerate, occupying the lowest quantum states with one fermion each up to the quantum state with Fermi energy E_F[1]. A prominent example for this behaviour are the conduction electrons in solids which are already degenerate at room temperature.

But to achieve these low temperatures in atomic gases, one first had to develop appropriate experimental tools to cool and trap atoms. Milestones on this way have been the invention of laser cooling, which lead to the development of Zeeman slowers [7] and the subsequent trapping of atoms in optical molasses [8], magneto-optical traps [9] and further in magnetic traps. The last step towards BEC has finally been the development of evaporative cooling, which uses the fact that a system's temperature is connected to its mean kinetic energy. Hence by removing atoms with energies above the mean kinetic energy from a sample, the mean kinetic energy and therefore the temperature decreases after thermalisation.

In 1995, these inventions finally led to the generation of the first BECs in ultracold atomic gases by *E. A. Cornell* and *C. E. Wieman* at Boulder [10] and independently by *W. Ketterle* at MIT [11]. The importance of this achievement for quantum physics is reflected by the fact that all of them were rewarded the Nobel prize already in 2001.

With such condensates, one was for the first time able to directly observe quantum mechanical behaviour, like matterwave interference [12] or tunneling processes [13] on a mesoscopic scale.

A further reason for the success of experiments with ultracold atoms is the existence of the so-called Feshbach resonances which were first observed experimentally in the group of *W. Ketterle* [14]. The power of these Feshbach resonances lies in the fact that one is able to tune the interaction strength of the atoms over a wide range, even from attractive to repulsive, by applying an external magnetic field. This makes it possible to investigate a system's properties for different interaction regimes and thus ultracold quantum gases provide the opportunity to check theoretical models in a very clean and controllable environment with many experimentally tunable parameters like temperature, interaction strength or atom number.

The use of these Feshbach resonances can for example be seen for ultracold Fermi gases. After the first creation of a degenerate Fermi gas by *Deborah Jin* at JILA in 1999 [15][2], one has been able to map out experimentally the crossover from the regime with attractive interactions, the BCS[3] side, to the regime with repulsive interactions, the BEC side using a Feshbach resonance [17]. By ramping the system onto the BEC side of the Feshbach resonance, one was also able to create weakly bound molecules composed of two fermions [18] and to achieve BEC of these molecules [19, 20, 21].

---

[1] for $T > 0$ the distribution is smoothened around E_F

[2] for Fermi gases some difficulties occur compared to the case of bosons since evaporative cooling is less effective due to the Pauli exclusion principle

[3] in this regime superfluidity can be described by the theory of J. Bardeen, L. N. Cooper and J. R. Schrieffer [16]

Another good example for the power of Feshbach resonances is the mimicing of other quantum systems, which are not easily accessible to investigation. In our experiment, we plan to investigate the behaviour of polarons, a quasi-particle known from solid state physics: when an electron moves through a crystal, it interacts with the surrounding ions of the crystal lattice due to Coulomb interactions. Thus when the electron passes, the lattice is distorted and hence lattice excitations, described by phonons, are induced. When diagonalizing the Hamiltonian of this system, the polaron, consisting of the electron and the induced phonons, is introduced. Attributed to this polaron is an effective mass which is larger than the sole electron mass, since the interaction with the lattice is attractive. But the investigation of polarons in solid state systems is not simple since the lattice spacings are on the order of Å and thus high resolution is needed. In addition, the interaction strength of the electron with the lattice phonons and thus the coupling of the phonon is given by the materials involved and can not be tuned. This tunability however is the large advantage of ultracold atoms, since here one can check theoretical models over a wide regime of coupling strengths, using Feshbach resonances.

In our case we will use a sodium BEC as a background sea in which we immerse a minority of fermionic lithium atoms. When interacting with the BEC, the fermions will alter the excitation spectrum, the so-called Bogoliubov modes [22], of the BEC, which can be mapped onto the phonons in the solid state case. The fermions correspond to the electrons and thus we can map our system onto the polaron Hamiltonian. Thus by using Feshbach resonances and alter the interaction strengths between the fermions and the bosons of the BEC, we will be able to investigate polarons for different coupling regimes including strong couplings which can not be observed in solid state physics. Our main goal is to determine the effective mass of these polarons and thus verify theoretical simulations which were done for example using a Feynman path-integral method by [23] and using mean-field theory in the PhD thesis of Jens Appmeier [24].

Outline of the thesis

This thesis reports on our first cooling step for lithium - the trapping of lithium atoms in a magneto-optical trap. Chapter 2 introduces the basic properties of the electronic states of alkali atoms and their behaviour in external magnetic fields. The manipulation of these electronic states is used for the frequency stabilisation of our master laser, which is explained in detail in chapter 3. This frequency standard is used to create a laser system for cooling and trapping lithium atoms. The basics of laser cooling are presented in chapter 4, with a focus on our spin-flip slower. In addition, the absorption imaging technique, which we use to probe trapped atom clouds, is explained in detail. At last, in chapter 5, our experimental results are presented. The first part describes the influence of the slower and oven parameters on the properties of our MOT and the second part contains atom number calibrations of our MOT using the absorption imaging technique intoduced in chapter 4.

2. Atomic Properties of Alkali atoms

This chapter introduces briefly the main features of alkali atoms and motivates why they are commonly used in atomic physics. As a reminder, the common notation to indicate the electronic state of an alkali atom is given. In addition, the *Hyperfine structure* is introduced since it splits up the *Fine structure* further and thus affects the energy spacing between different electronic states. The energy shift of alkali atoms in an external magnetic field is also shortly discussed. Finally, the m_F-selection rule for optical dipole transitions is given and its consequences shortly discussed.

2.1. Alkali atoms

The basic feature of alkali atoms is that they have only one unpaired electron and thus a total electron spin $S = 1/2$ in their outer shell. In the atom's ground state this electron is in the S-shell, which corresponds to an orbital angular momentum $L = 0$. Thus the total electron angular momentum[1] adds up to $J = 1/2$. The ground state of an alkali atom can hence be written as $n^2 S_{1/2}$ in the common notation[2] where n denotes the main quantum number of the atom. The ground state of lithium can for example be written as $2^2 S_{1/2}$. In the first excited state, an alkali atom has its unpaired electron in the P-shell ($L = 1$). Thus the orbital angular momentum can couple to the electron spin either parallel ($J = 3/2$) or anti-parallel ($J = 1/2$) [25]. This leads to a splitting of the excited state into $n^2 P_{3/2}$ and $n^2 P_{1/2}$. In the case of lithium, the splitting is on the order of $10\,\mathrm{GHz}$ (see Figure 2.1). For all alkalis, the energy splitting between the ground state and these excited states lies in a range where lasers are available, for example $670.977\,\mathrm{nm}$ in lithium between $2^2 S_{1/2}$ and $2^2 P_{3/2}$. In atomic physics, the transitions $n^2 S_{1/2} \rightarrow n^2 P_{3/2}$ are of particular interest due to reasons which will be explained in chapter 2.4. These transitions are called the D_2-lines whereas the transitions $n^2 S_{1/2} \rightarrow n^2 P_{1/2}$ are called the D_1-lines.

2.2. Hyperfine Interaction

Until now the atom's nucleus has been assumed to be point-like, of infinite mass and without any angular momentum of its own. When one skips these assumptions, two effects are observable. One effect is that the Fine structure levels are shifted due to the finite volume of the nucleus and its interaction with the surrounding electrons. These shifts are known as *Isotope shifts*, since different isotopes of the same atom

---

[1] J results from the spin-orbit coupling of the atom, which leads to an energy splitting $\Delta E \propto \vec{L} \cdot \vec{S}$ of the electronic states, the so-called *Fine structure*

[2] $n^{2S+1}[L]_J$, where $[L] = 0, 1, 2$ corresponds to the S-, P-, D-shell

have different masses and a slightly different charge distribution in the nucleus [26]. This difference can be verified experimentally, for example with ^{85}Rb and ^{87}Rb [27]. The second effect is the so-called *Hyperfine splitting*. This splitting occurs since the nucleus also has a spin $\vec{I}$ and connected to it a magnetic moment $\vec{\mu}_I$, which is much smaller than the Bohr magneton μ_B. The nuclear spin $\vec{I}$ couples to the total angular momentum $\vec{J}$ and induces thus the energy shift $\Delta E \propto \vec{J} \cdot \vec{I}$. In analogy to the spin-orbit coupling one introduces the total angular momentum $\vec{F} = \vec{I} + \vec{J}$. It can therefore take values of

$$F = |j - I|, |j - I| + 1, ..., j + I$$

In our experiment we use the fermionic isotope ^{6}Li , to which we will refer from now on only as lithium, with nuclear spin $I = 1$. Thus the ground state splits up into $F = 1/2$ and $F = 3/2$. The corresponding energy splitting is 228.2 MHz and hence much smaller than the splitting induced by the Fine structure (see Figure 2.1 (left)). This is due to the small magnetic moment of the nucleus μ_I compared to μ_B. In addition one observes that for $P_{3/2}$ the Hyperfine splitting between the $F = 5/2$ and the $F = 1/2$ state is $2\pi \times 4.4$ MHz which is smaller than the natural linewidth $\Gamma = 2\pi \times 5.8724$ MHz of Lithium (see Appendix A). Therefore when exciting a free atom[3] from one of the Hyperfine ground states to $^{2}P_{3/2}$, in most cases there is more than one possible excitation obeying the selection rules (see section 2.4). Hence, without an external magnetic field, the $P_{3/2}$ state can be considered as one energy level.

2.3. Zeeman Effect

When applying an external magnetic field $\vec{B}$[4] one introduces the so-called quantization axis $\vec{e}_z$. The projections of the angular momenta $\vec{S}, \vec{L}, \vec{J}, \vec{I}, \vec{F}$ onto this axis are quantized with values $i_z = m_i \cdot \hbar$ and magnetic quantum numbers $m_i = -i, -i + 1, ..., i$[5]. The coupling of the angular momenta to an external magnetic field differs for different magnetic quantum numbers and leads to an energy splitting of these substates. This dependence was first observed experimentally by P. Zeeman [28]. The couplings can be described as a perturbation

$$\hat{H}_{Zeeman} = -\mu_B \cdot B \cdot (g_S \hat{S}_z + g_L \hat{L}_z + g_I \hat{I}_z)$$

of the atomic Hamiltonian $\hat{H}_0$ where the g_i-factors (see Appendix A) connect the projected averaged magnetic moments $\langle \vec{\mu}_i \rangle_z$ with the Bohr magneton μ_B. As long as the coupling energy E_{couple} between $\vec{J}$ and $\vec{B}$ is much smaller than the energy of the Hyperfine coupling E_{HFS} we are in the Zeeman regime (see Figure 2.1 (right)). In this regime, the coupling between $\vec{J}$ and $\vec{I}$ is sustained and the energy shift can be calculated using first order perturbation theory to be [29, 26]

$$\Delta E_{Zeeman} \approx g_F \cdot \mu_B \cdot m_F \cdot B. \tag{2.1}$$

---

[3]free means that no external magnetic field is applied
[4]without loss of generality we always assume $\vec{B} = B \cdot \vec{e}_z$
[5]i is a placeholder for the different angular momenta
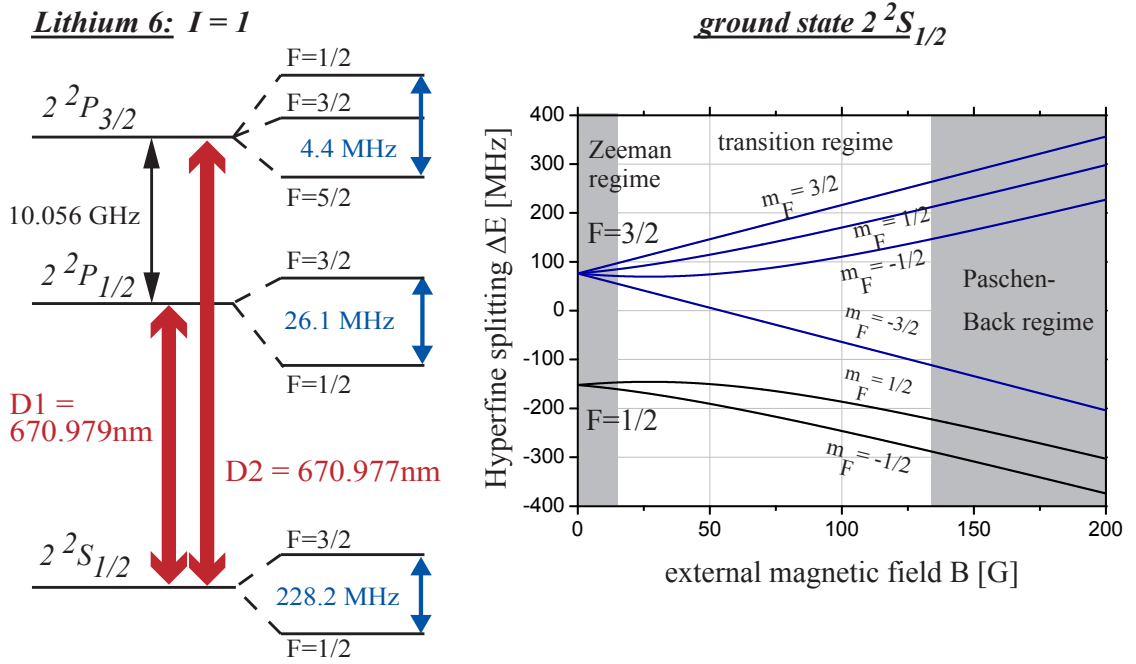
Figure 2.1.: *Hyperfinestructure of* ^{6}Li *(left) and the energy splittings due to the Zeeman effect for the Hyperfine ground states of* ^{6}Li *(right).*

For $E_{\text{couple}} >> E_{\text{HFS}}$, the Paschen-Back regime (see Figure 2.1 for the case of ^{6}Li), the coupling between $\vec{J}$ and $\vec{I}$ is no longer sustained and F is no longer a good quantum number[6]. In analogy to equation 2.1 the energy shifts can then be calculated to be [30]

$$\Delta E_{Paschen-Back} \approx \mu_B \left(g_J \cdot m_J + g_I \cdot m_I \right) B, \qquad (2.2)$$

where the second term plays only a role for large magnetic fields, since $g_I << g_J$ (see Appendix A).

As one can see in Figure 2.1, the Hyperfine coupling is in most cases already canceled at quite low magnetic fields which can easily be produced in the laboratory. This is in contrast to the Fine structure where $\vec{J}$ is only decoupled for magnetic fields of some Tesla. For lithium, we are in most cases in the transition regime between the Zeeman and the Paschen-Back regime. The energy shift has then to be calculated numerically using the Breit-Rabi formula [29, 26]. In Figure 2.1 a numerical calculation for the ground state $^2S_{1/2}$ is depicted (taken from [30]).

---

[6]good quantum numbers give a set of eigenfunctions in which the Hamiltonian can be diagonalized

2.4. Light polarisation and selection rules

In atomic physics the circular polarisation of a laser beam is in most cases not characterized with respect to its wavevector $\vec{k}$[7], but to the direction of an external magnetic field $\vec{B}$. A beam propagating along $\vec{B}$ has σ^+-polarisation if its chirality is right-handed and σ^--polarisation if it is left-handed (see Figure 2.2). A linearly polarised beam has π-polarisation and can also result as a superposition of a σ^+- and a σ^--beam.

$\vec{B}$

$\vec{k}$ $\vec{k}$ $\vec{k}$

σ^+ - polarisation σ^- - polarisation π - polarisation
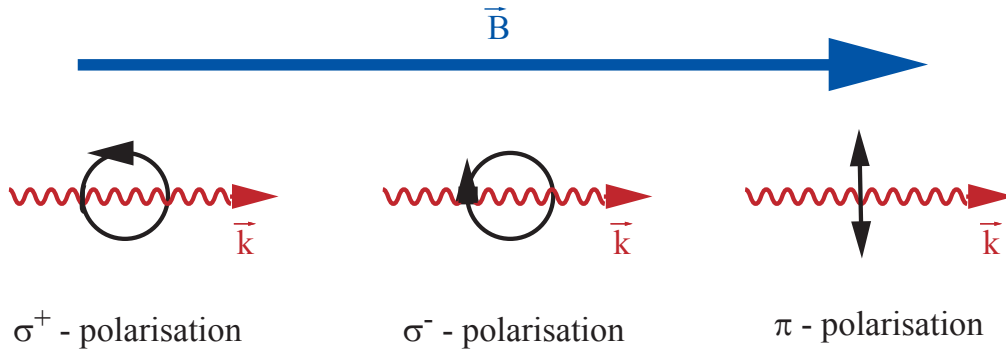
Figure 2.2.: *The different possible polarisations of a laser beam relative to a magnetic field.*

In optical dipole transitions, the magnetic quantum numbers m can only change by $\Delta m_F = 0, \pm 1$ in the Zeeman regime or $\Delta m_J = 0, \pm 1$ and $\Delta m_I = 0$ in the Paschen-Back regime [31]. The induced transition depends on the polarisation of the photon involved. In an absorption process, for σ^+-polarisation we get $\Delta m = +1$, for σ^--polarisation $\Delta m = -1$ and for π-polarisation $\Delta m = 0$. In addition, $\Delta F = 0, \pm 1$ must be fullfilled whereas $F = 0 \rightarrow F' = 0$ is forbidden. The same rule applies for J in the Paschen-Back regime.

Considering these selection rules, it is suggestive to use the D_2-line for laser cooling. In this case we can excite the so-called 'fully stretched states', where all the angular momenta are parallel $\Rightarrow |m_F| = F = j + I = l + s + I$. When for example irradiating σ^+-light without an external magnetic field, atoms from the ground state $|F = {}^3\!/\!_2, m_F = {}^3\!/\!_2\rangle$ can only be excited to $|F' = {}^5\!/\!_2, m_{F'} = {}^5\!/\!_2\rangle$. Due to the transition rules, the atoms can then only decay back into the ground state $|F = {}^3\!/\!_2, m_F = {}^3\!/\!_2\rangle$ and and one has no losses to other states. These transitions are called 'closed transitions' and are hence widely used in laser cooling as can be seen in chapter 4.

---

[7] $\left|\vec{k}\right| = \frac{2\pi}{\lambda}$

3. The Lithium Master Laser

In order to be able to cool and trap lithium atoms (see chapter 4), we need a stable laser source with a narrow linewidth at about 670.977 nm to excite the D_2-line of lithium. We therefore use a grating-stabilised diode laser because of its dynamic tunability and reliability.

This chapter explains the principles of a grating stabilised laser diode. Our diode mount is shown and a scheme to adjust the wavelength within an accuracy of 0.7 GHz with the help of a wavemeter[1] is presented. In addition, the principle of Doppler-free spectroscopy, including our used setup, is described. Further, the derivation of our error signal from the spectroscopy signal, and how it is used to stabilise the laser, is explained. At last a short overview is given how the master laser is used to lock a second laser, the slave laser, with an offset onto the master laser and how the beams for cooling and trapping are prepared.

3.1. Grating-stabilized diode laser

Laser diodes are nowadays available for many wavelengths and are thus widely used in atomic physics. In principle, they consist of a n- and p-type semiconductor with an active region in between. The facets of the diode have a high reflectivity and thereby form a cavity. When sending a current through the diode, it begins laser action above a certain threshold current I_{th}. The emitted wavelength depends mainly on the used semiconductor material but is also very sensitive to the current density j_{LD} and the temperature inside the diode. However, a free running laser diode has two major disadvantages, namely its large linewidth and the poor tunability. But since a laser diode is highly sensitive to optical feedback, these problems can be solved with the help of an external resonator. We use the Littrow configuration which is sketched in Figure 3.1 and uses a grating to reflect the laser beam. Optical feedback is then achieved when the first order is reflected back to the diode and the zero order is outcoupled from the system. Hence the external resonator is formed by the grating and the rear facet of the laser diode [32].

The wavelength λ of the outcoupled beam can then be tuned by varying the angle Θ of the grating. This comes from the fact that at a given Θ, the incoming and reflected beam are superimposed only for $\lambda = \frac{2\sin\Theta}{m}$ where m is the number of lines per unit length of the grating. With this technique a linewidth less than 100 kHz can be achieved.

---

[1] A tool to measure the wavelength of a beam. We use the *Coherent Wavemaster*.
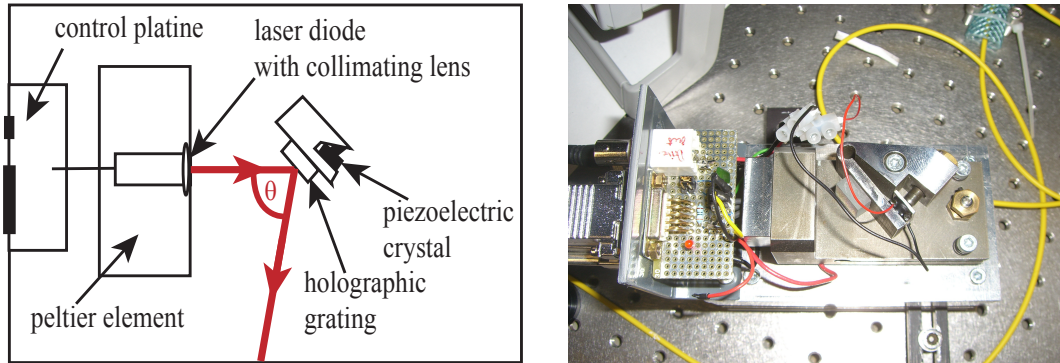
Figure 3.1.: *Sketch of the Littrow configuration (left) and a picture of our current laser diode mount (right)*

3.1.1. Laser diode mount

In Figure 3.1, a picture of our current laser diode mount is shown. We use the Toptica #LD-0675-0030-1 laser diode with an output power of about 30 mW at a center frequency of 675 nm. Since fluctuations in the current and temperature directly manifest themselves in the emitted frequency, these fluctuations have to be very small. Hence, the current is controlled with the Thorlabs LDC 201 C and the temperature is regulated with a peltier element which is controlled by the Tektronix TED 200. The used diode proves to be very stable and shows no hysteresis effects or drifts when turning it on and off and thus allows for day to day reproducability. The laser diode is put into a lens tube with a collimator lens to compensate the beam divergence of the laser diode. The lens tube is then build into a block of 'Neusilber' which in turn is put onto a peltier element. The grating is attached to a lever arm which can be either turned coarsely with a fine thread screw or more precisely with a high-voltage piezoelectric crystal. The platine in front of the laser diode contains the connector pins for the laser diode and is connected to the LDC by a 9-pin D-sub jack. In addition, a Bias-T has been soldered onto the platine, which enables us to modulate the laser current with radio frequencies[2]. The peltier element is also connected to the TED with a 9-pin D-sub jack and the piezoelectric crystal has a BNC input.

3.1.2. Tuning the diode lasers wavelength

The wavelength emitted by our grating-stabilized diode laser is determined by the overlap of the different gain profiles. In Figure 3.2, these gain profiles and the resulting mode structure are depicted. The center frequency of the grating profile depends on the grating angle Θ and its width is determined by the grating quality $\frac{\nu}{\Delta\nu} = N$ where N is the number of lines which are illuminated by the beam. In our experiment we use a grating with $m = 1800 \frac{\text{lines}}{\text{mm}}$ and our beam width B is

---

[2]this is a relict from our first design
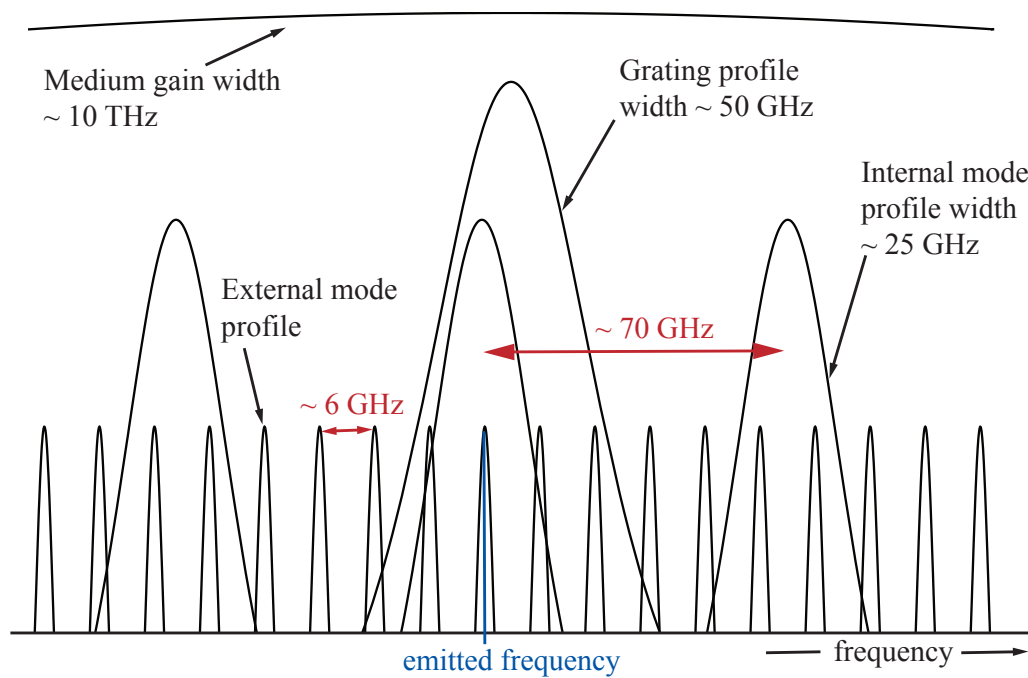
Figure 3.2.: *The overlap of the different gain profiles determine the emitted frequency. The spacings between the modes are measured with a wavemeter.*

approximately $5\,\mathrm{mm}$. Therefore $N = B \cdot m$ and at our desired wavelength of $670.977\,\mathrm{nm}$ we obtain $\Delta\nu = \frac{\nu}{N} = \frac{c}{B\,m\,\lambda} \approx 50\,\mathrm{GHz}$. By roughly changing the angle of the grating one can therefore jump between different internal modes and the mode spacing is measured using a wavemeter to be approximately $70\,\mathrm{GHz}$.

As mentioned at the beginning, the diode laser can be seen as a cavity with an internal mode profile which depends on the current density and the temperature inside the diode. When altering the injected current, the refraction index inside the diode changes and the internal modes are shifted. Thus by altering the laser current one is able to jump between the external modes.

The external resonator, defined by the grating and the rear facet of the diode, has a length $L_{\mathrm{ext}} \approx 2.5\,\mathrm{cm}$ and thus a mode spacing of about $\mathrm{FSR} = \frac{c}{2\,L_{\mathrm{ext}}} = 6\,\mathrm{GHz}$. This is also verified experimentally by altering the laser current and measure the resulting mode jumps with a wavemeter.

To obtain our desired wavelength within an accuracy of $\Delta\lambda = 0.001\,\mathrm{nm}$ or corresponding $0.7\,\mathrm{GHz}$, we use the following scheme:

1. Adjust the grating angle: alters λ in steps of about $\Delta\lambda = 0.1\,\mathrm{nm}$ or accordingly $\Delta\nu = 66.6\,\mathrm{GHz}$

2. Adjust the laser current I_{LD}: alters λ in steps of about $\Delta\lambda = 0.01\,\mathrm{nm}$ or accordingly $\Delta\nu = 6.6\,\mathrm{GHz}$

3. Regulate the diode temperature: alters λ on the order of $\Delta\lambda = 0.001\,\mathrm{nm}$ or accordingly $\Delta\nu = 0.7\,\mathrm{GHz}$

But this is only a rough starting point to find our spectroscopy signal (see section 3.2). With the help of a piezo crystal which alters the angle of the grating and thus also the length of the external resonator, we can then scan our wavelength continuously over a range of $4 - 5\,\mathrm{GHz}$ without any mode jumps by fine adjusting the grating. This scan range could be enlarged with the help of a *Feed Forward*. A Feed Forward simply scans the current simultaneously to the grating and thereby shifts the internal modes at the same rate as the external modes. Thus mode jumps are prevented and the scan range is improved. The problem however is to find the right proportionality between scanning the grating and the current. Since the spectrum we want to observe has a width smaller than $0.5\,\mathrm{GHz}$, we operate our diode laser without a Feed Forward.

3.2. Doppler-free saturation spectroscopy of lithium

In order to get a stable laser system, we need a frequency standard on which we can lock our laser. A natural way is to choose an atomic transition of the used species. Since lithium has a low vapour pressure compared to other alkalis we have to build our own spectroscopy cell which we can heat up to temperatures of about $400\,°\mathrm{C}$ [33]. This is in contrast to e.g. rubidium where one can just buy a simple spectroscopy cell and do not have to put any effort into it. In order to avoid coating of the glass windows with lithium, the buffer gas argon has been inserted into the spectroscopy cell to decrease the mean free path of the lithium atoms. For temperatures above
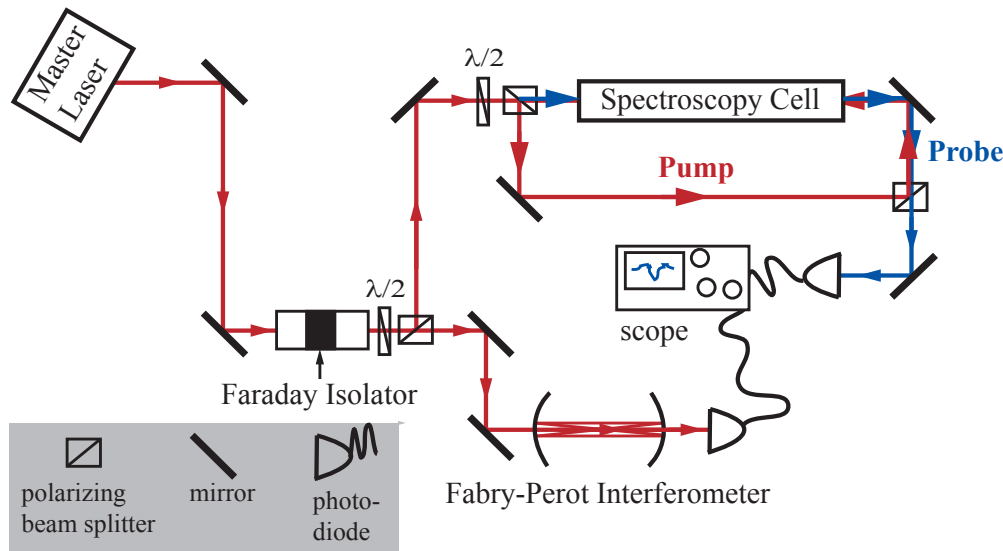
Figure 3.3.: *Setup for doppler-free saturation spectroscopy of* ^{6}Li.

some kelvin, the atomic transisitons are already strongly broadened by the Doppler effect [25] on the order of GHz and thus we have to use doppler-free saturation spectroscopy to resolve the Hyperfine structure of lithium.

In this section, an intuitive picture of doppler-free saturation spectroscopy is given for the case of lithium. For a more general description one can refer to [34]. A

schematic of our used spectroscopy setup can be seen in Figure 3.3. In essence, one splits the laser beam into two beams, probe and pump, by a polarizing beam splitter (PBS). The two counterpropagating beams are then superimposed inside the spectroscopy cell and therefore an atom with the velocitiy v sees an opposite doppler shift for the two beams[3]. At last, the signal of the transmitted probe beam is captured on a photodiode (Thorlabs DET36A) and observed with a scope. To check wether our laser operates in single mode, we also installed a Fabry-Perot interferometer (FPI) in confocal mode [35].

Without an external magnetic field, the D_2-line is in essence a three level system since the Hyperfine states of the excited state $2^2 P_{3/2}$ are not resolved (see section 2.2). For simplicity we will denote the excited state $2^2 P_{3/2}$ as $|e\rangle$ and the ground states $|2^2 S_{1/2}, F = 3/2\rangle$, $|2^2 S_{1/2}, F = 1/2\rangle$ as $|g_1\rangle$ and $|g_2\rangle$, respectively. The transition frequencies from the ground states to the excited state are denoted with ω_1 and ω_2.

To understand the shape of the transmitted signal one has to differentiate between different cases which are depicted in Figure 3.4.

Figure 3.4.: *Three possible absorption schemes in doppler-free saturation spectroscopy. The blue rippled lines indicate the pumping processes by spontaneous emission.*

(a) When exciting the atom with an arbitrary frequency ω, there is for example one velocity class v for which the probe beam ($\omega_{\text{Probe}} = \omega - k \cdot v$) is in resonance with the atomic transition $|g_1\rangle \rightarrow |e\rangle$. But the pump beam ($\omega_{\text{Pump}} = \omega + k \cdot v$) is then out of resonance to this transition and hence the probe beam is unaffected by it. In this case one gets a normal absorption of the probe beam with a broad Doppler profile on the order of some GHz.

(b) For $\omega = \omega_1$, the velocity class $v = 0$ is resonant with $|g_1\rangle \rightarrow |e\rangle$ for both probe and pump beam. Atoms excited by the pump beam can then decay by spontaneous emission into the 'dark' state $|g_2\rangle$ which is not resonant with either

---

[3]in the following considerations, v is always assumed to be parallel to the beams

of the beams for $v = 0$. Thus the absorption of the probe beam is attenuated since there are less atoms in $|g_1\rangle$ with $v = 0$, due to this pumping process. The transmission signal is thus enhanced and has a sharp peak with a width at the order of the natural linewidth[4]. Of course, similar arguments also hold for $\omega = \omega_2$.

(c) For $\omega = \frac{\omega_1 + \omega_2}{2}$ one gets an additional feature. In this case, the pump beam is for example resonant with the transiiton $|g_2\rangle \to |e\rangle$ for the velocity class $v = \frac{\omega_2 - \omega_1}{2\,k}$. Thus the pump beam can 'shovel' atoms from $|g_2\rangle$ to $|g_1\rangle$. In $|g_1\rangle$, these atoms are now resonant with the probe beam and are also excited. The absortion is therefore enhanced and one observes a minimum in the transmission signal, the so-called crossover peak. Of course, similar arguments also hold for the velocity class $v = -\frac{\omega_2 - \omega_1}{2\,k}$.

In Figure 3.5, a measurement of our spectroscopy signal can be seen. The Hyperfine structure is resolved and we can observe the three peaks for the different frequencies mentioned above. The relative strength of these transitions can be understood by the different degeneracy of the Hyperfine ground states, whereas $|g1\rangle$ has two and $|g_2\rangle$ has four magnetic substates. Thus the peak caused by $|g_1\rangle \to |e\rangle$ is twice as large as the one caused by $|g_2\rangle \to |e\rangle$. For the crossover peak the substates of both ground states are involved, thus it is thrice as large as the peak $|g_2\rangle \to |e\rangle$. The energy splitting between the ground states is 228.2 MHz and thus the width of these peaks can be estimated to be roughly 30 MHz, approximately five times the natural linewidth of lithium. This broadening is mainly caused by collisions with the buffer gas argon. One hence has to find a trade-off between small, narrow peaks and avoiding the coating of the glass windows of our spectroscopy cell.
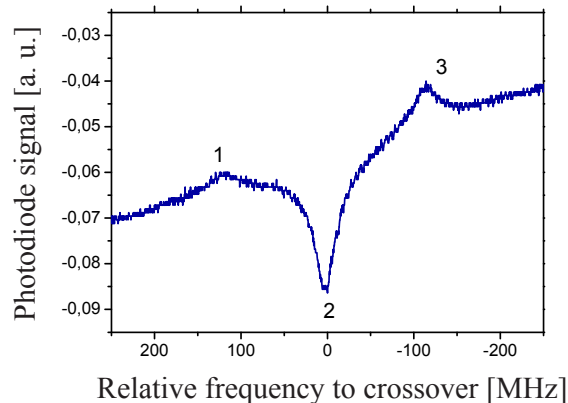
Figure 3.5.: *The spectroscopy signal for lithium: 1 denotes the $|g_2\rangle \to |e\rangle$ transition, 3 the $|g_1\rangle \to |e\rangle$ transition and 2 the crossover*

---

[4]it is also broadend due to collisions with the buffer gas argon and saturation broadening [34]

3.3. Frequency stabilisation of the master laser

As a frequency standard for our master laser, we naturally choose the crossover peak since it is the most distinctive feature in the spectrum. To lock the laser, we have to give a feedback to the piezoelectric crystal. This feedback must contain information on which side of the crossover the current frequency is. The spectroscopy signal itself is hence not suited to this task since it has the same sign on both sides of the crossover peak. But the derivative of the signal fullfils this necessary condition and will be used to lock the laser. In the following it will be explained how one can produce the error signal with electronics and how we finally lock our master laser onto the crossover peak.

3.3.1. Producing the error signal

We use frequency modulation (FM) of our laser to produce the error signal. This can be done by modulating the laser current[5], which results in a FM with amplitude $\Delta\omega$ and modulation frequency ω_{LO}. For $\Delta\omega << \Gamma$, the modulation can be intuitively
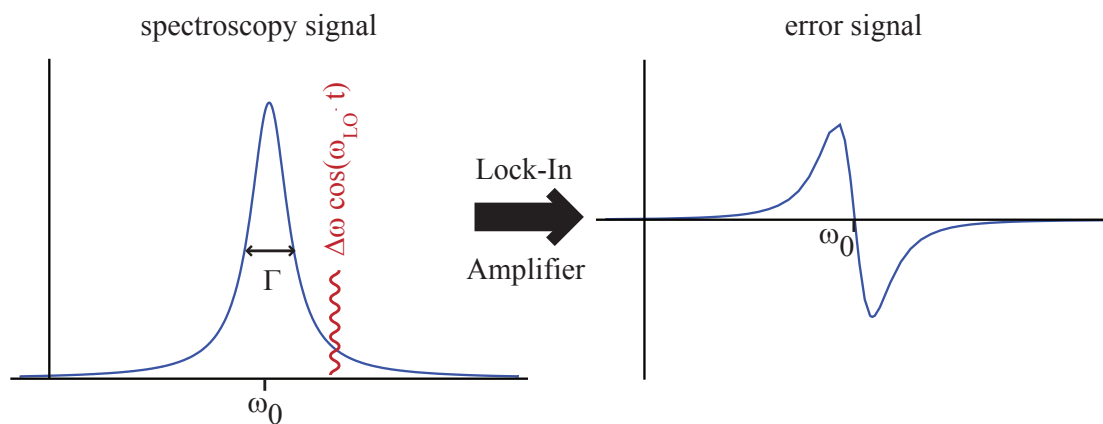
Figure 3.6.: *Generation of the error signal by frequency modulation of the laser.*

understood as wiggeling the frequency around a center frequency ω and thus scanning the vicinity of the lineshape $f(\omega)$ which is depicted in Figure 3.6. Since the amplitude is small, the deviation caused by the wiggeling can be expanded in a Taylor series of first order and thus will be proportional to its derivative

$$f(\omega + \Delta\omega \cos(\omega_{\mathrm{LO}} \cdot t)) \approx f(\omega) + f'(\omega)\Delta\omega \cos(\omega_{\mathrm{LO}} \cdot t). \tag{3.1}$$

The term proportional to the derivative can now be extracted from the signal using a lock-in amplifier (see Figure 3.6). A lock-in amplifier is essentialy a very narrow bandpass with a tunable frequency which also provides a gain. Thus one is able to extract even very small signals overlaid with noise.

[5]in our setup this is done with a Voltcraft 7207 function generator which is connected to the Modulation Input of the Laser Diode Controller (see Figure 3.8)

This filtering is done by first mixing the input signal f_{inp} coming from the photodiode with a reference frequency, in our case $\cos{(\omega_{\text{LO}} \cdot t)}$[6], and then sending this signal through a low pass filter with cut-off frequency ω_c. The low pass can be mathematically described as the time integral

$$\frac{1}{\tau} \int_0^\tau \mathrm{d}t \cos{(\omega_{\text{LO}} \cdot t)} \cdot f_{\text{inp}} \tag{3.2}$$

with time constant $\tau = \frac{1}{\omega_c}$. When inserting the Taylor expansion from (3.1) into (3.2), we obtain

$$\frac{1}{\tau} \int_0^\tau \mathrm{d}t \left[\cos^2(\omega_{\text{LO}} \cdot t) f(\omega) + \cos{(\omega_{\text{LO}} \cdot t)} \Delta\omega f'(\omega) \right]. \tag{3.3}$$

For $\omega_{\text{LO}} >> \omega_c$, the term in (3.3) oscillating with $\cos{(\omega_{\text{LO}} \cdot t)}$ will vanish after the integration and only the term proportional to $\cos^2(\omega_{\text{LO}} \cdot t)$ will survive. Thus the output signal will be proportional to the derivative $f'(\omega)$

$$f_{\text{out}} \propto \Delta\omega \cdot f'(\omega). \tag{3.4}$$

The choice of τ will also determine how much noise is filtered. A large τ will on the one hand filter more noise but on the other hand limit the reaction time of the lock-in to changes in the signal. Thus we have to find a trade-off between low noise and still seeing the derivative of the spectroscopy signal. A typical error signal is shown in Figure 3.7. One clearly sees the derivatives of the three peaks with different amplitudes and a different sign of the crossover slope.
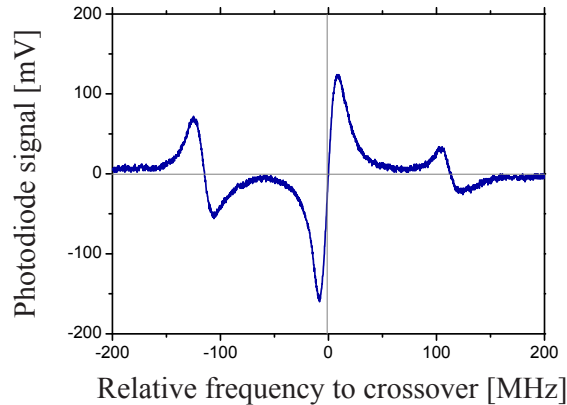
Figure 3.7.: *Typical error signal for our setup. The width of the crossover is approximately 18 MHz.*

---

[6]in reality there is also a phase difference Φ between the input signal and the reference signal but it can be compensated with a phase shifter at the lock-in amplifier. Thus we omit Φ in the following calculations for the sake of simplicity.

3.3.2. Locking scheme

Our locking scheme is depicted in Figure 3.8. The output of a Loop Amplifier is given to the piezoelectric crystal on the diode laser mount. The Loop Amplifier is fed by an an external sweep signal and can control both the offset and the amplitude of the signal which corresponds to the scan range of the laser frequency. Thus, by simultaneously decreasing the scan range and adjusting the offset, one can zoom the scan of the laser frequency into the crossover region. In addition, the Loop Amplifier gets the error signal from the lock-in amplifier as an input. This input can be given as an integration and/or proportional feedback[7] to the output and hence to the piezoelectric crystal. Thus after zooming into the crossover peak and adjusting the scan range to zero, the laser can be locked by turning on the feedback. When locked, we measure a peak-to-peak noise of about 12 % of the height of the crossover slope. Our achievable lock stability is therefore better than 1.2 MHz.
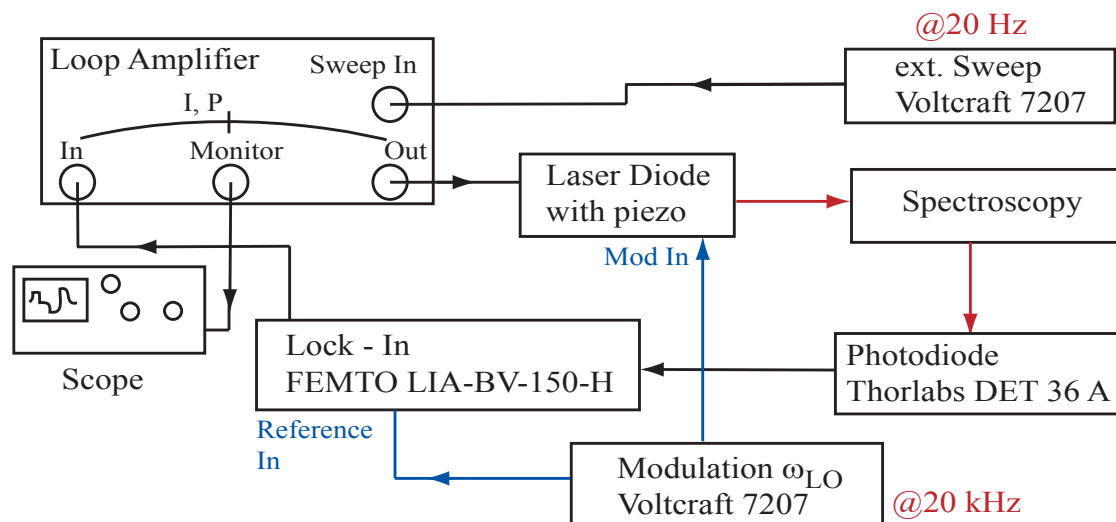
Figure 3.8.: *Schematics of the locking scheme*

3.4. Preparation of the laser beams for cooling and trapping

Since the master laser has only an output power of some mW, we need a second laser, the slave laser, with higher power which can be locked onto the master laser. Therefore we use a Tapered Amplifier system (TA) from Toptica with an output power of about 400 mW which is beat locked onto the master laser with an adjustable detuning [36]. The output beam from the TA is then divided into several beams for cooling and trapping with polarizing beam splitters and these individual beams are shifted in frequency with the help of acusto-optic modulators (AOM's) as described

---

[7]integration Feedback is essential since it can nullify the deviation. The proportional feedback can be turned on in addition for a faster regulation.

in detail in [36]. At the end, the individual beams are guided from the optical table to the experiment with glass fibers .

4. Experimental Techniques to Cool and Image Atoms

In our experiment, the first step to cool lithium is to trap it in a magneto-optical trap (MOT) [9, 31]. In order to achieve this, we first have to prepare an atomic beam of lithium and cool the atoms inside it from an initial maximal velocity of about $v_{\mathrm{max}} \approx 700 \, \frac{\mathrm{m}}{\mathrm{s}}$ to an end velocity of about $v_{\mathrm{end}} \approx 30 \, \frac{\mathrm{m}}{\mathrm{s}}$. This has to be done, since otherwise the atoms in the beam would be too fast for the MOT to trap them.

This chapter explains the experimental steps needed to obtain an atomic beam of cool, trappable atoms from a reservoir of solid lithium. In addition, the absorption imaging technique as an experimental tool to probe atom clouds is introduced.

4.1. Preparing the atomic beam

For laser cooling which will be introduced in section 4.2, we need a gas in an ultra-high vacuum because otherwise the atoms would collide with background gas and thus heat up. But to obtain a decent amount of gaseous lithium, we first have to heat up a lithium reservoir to temperatures on the order of $550 \, ^\circ \mathrm{C}$. For this purpose we use a two-species oven (Figure 5.1 (a)) [37] where lithium and sodium can be heated independently of each other.
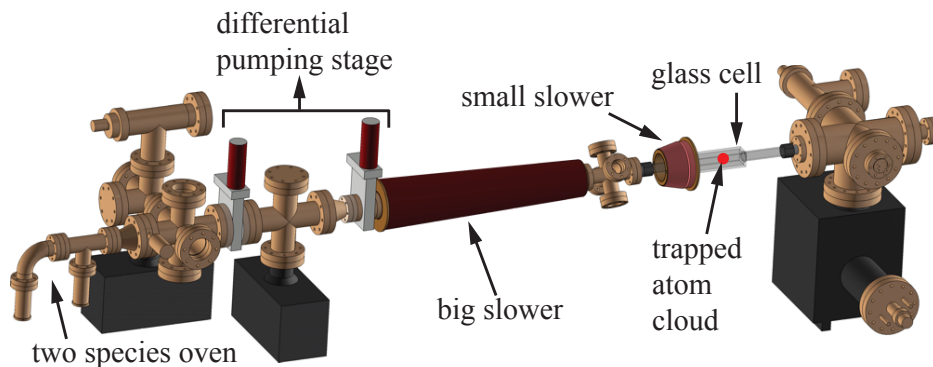
Figure 4.1.: *Schematic of our laser cooling setup (modified from [38])*

The heating temperature for sodium is smaller ($\approx 350 \, ^\circ \mathrm{C}$) compared to lithium due to the low vapour pressure of lithium. After mixing both species inside the mixing chamber, the atoms pass the oven nozzle and are collimated furthermore with the help of a differential pumping stage. At the end we have a collimated atomic beam,

entering our slower coils and travelling towards the glass cell where our experiments are performed. A schematic of the whole setup can be seen in Figure 4.1.

4.2. Basics of laser cooling

The main idea behind laser cooling of alkali atoms is to decelerate them with momentum transfer of absorbed photons. When choosing the right polarisation and frequency of the laser beam, one can excite a closed transition (see section 2.4), and the atom can be regarded as a two level atom. An atom with momentum $\vec{p}_{\text{atom}}$, irradiated with a counterpropagating laser beam with wavevector $\vec{k}_{\text{laser}}$ (Figure 4.2 (a)), is excited, absorbing a photon and thus the momentum $\hbar \cdot k_{\text{laser}}$ (Figure 4.2 (b)). Since the photon is counterpropagating, the atom is slowed down. To absorb a further photon, the atom has to decay into its ground state. This can happen either by spontaneous or induced emission. When the atom decays by induced emission, the resulting momentum change of the atom is zero since the photon is emitted into the mode of the laser beam. But when decaying by spontaneous emission, the photon is emitted isotropically and thus the momentum of the atom is changed by $\Delta \vec{p}$ (Figure 4.2 (c)). But since the emission is isotropic, the resulting force on the atom due to
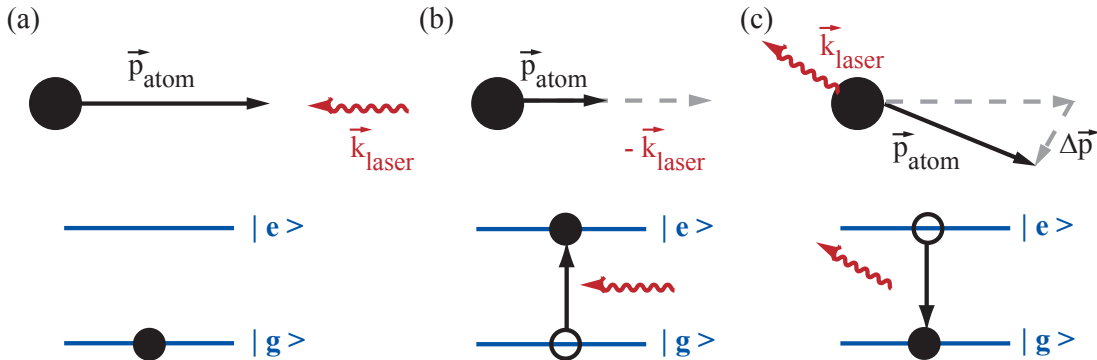
Figure 4.2.: *(a): an atom is irradiated by a counterpropagating laser beam*
            (b): absorption of a photon
            (c): spontaneous emission of a photon

spontaneous emission vanishes when averaging over many scattering processes and the atom only experiences a force F_{scatter} opposite to its initial momentum. This scattering force can be calculated as [31]

$$F_{\text{scatter}} = \frac{\mathrm{d}p_{\text{atom}}}{\mathrm{d}t} = \hbar \cdot k_{\text{laser}} \cdot \frac{\Gamma}{2} \frac{s_0}{1 + s_0 + (2\,\delta/\Gamma)^2}, \qquad (4.1)$$

where s_0 is the saturation of the transition, $\delta = \omega_{\text{laser}} - \omega_0$ the overall detuning of the irradiated beam and Γ the natural linewidth of lithium which determines the maximal scattering rate. The saturation parameter s_0 denotes the intensity I of the laser beam normalised by the atom's saturation intensity I_S (see Appendix A).

With equation (4.1) it is apparent that there is a maximal scattering force $F_{\text{scatter,max}}$ for infinite saturation s_0. For lithium we thus obtain a maximal deceleration of

$$a_{\text{max}} = \frac{F_{\text{scatter,max}}}{m_{\text{Li}}} = 1.82 \times 10^6 \, \frac{\text{m}}{\text{s}^2} \approx 2 \cdot 10^5 \, \text{g}, \tag{4.2}$$

where g is the gravitational acceleration on earth. Although the recoil momentum p_{rec} of a single photon for a lithium atom moving with $v = 700 \, \frac{\text{m}}{\text{s}}$ is only about $0.014\,\% \cdot p_{\text{atom}}$, the deceleration is still orders of magnitude larger than g, since the scattering rate is on the order of $10^7 \, \frac{\text{scattering porcesses}}{\text{s}}$ for a resonant beam with $s_0 = 1$. Hence, to decelerate such an atom to absolute halt, about 7000 scattering processes are needed which corresponds to a deceleration time $t_{\text{dec}} = 0.76 \, \text{ms}$.

However, until now we did not take a main feature of laser cooling, the Doppler effect, into account. An atom moving relative to a laser beam sees the frequency of the laser detuned [25, 31] with detuning

$$\delta_D = -\vec{k}_{\text{laser}} \cdot \vec{v}_{\text{atom}} = -k_{\text{laser}} \cdot v_{\text{atom}} \cdot \cos\phi,$$

where $\phi = \angle\left(\vec{v}_{\text{atom}}, \vec{k}_{\text{laser}}\right)$. In our case of a counterpropagating beam the angle is $\phi = 180°$ and thus

$$\delta_D = k_{\text{laser}} \cdot v_{\text{atom}}.$$

Hence, even when the atom is initially in resonance with the laser beam, it will drop out of resonance after a few collisions due to the detuning caused by the Doppler effect. To compensate this effect, several schemes have been developed over the past decades like e.g. [39, 40, 41, 42, 43]. In our experiment we use a so-called Zeeman slower which has been the first method to be experimentally realised [7].

An additional feature we take into account for our experimental implementation is the divergence of the atomic beam entering the Zeeman Slower. To achieve that the shape of the slower beam overlaps with the atomic beamand we are thus able to scatter all atoms, we first enlarge our slower beam with a telescope and then focus it using a lens with focal length $f = 3 \, \text{m}$ onto the entrance points of the Zeeman slower. Furthermore this compensates another effect: when approaching the entrance point of the Zeeman slower, the slower beam is absorbed and the saturation s_0 drops. The focusing of the slower beam hence increases the intensity and therefore s_0 in the vicinity of the entrance point.

4.3. Zeeman Slower: Resonance condition and ideal magnetic field

To prevent the atoms from dropping out of resonance during the slowing process, we make use of the Zeeman effect introduced in section 2.3. By applying a spatially varying magnetic field we can compensate the detuning of the laser frequency due to the Doppler effect by shifting the resonance frequency of the atomic transition. This compensation has to be fullfilled during the whole slowing process and can be

formally described with the resonance condition

$$
\begin{aligned}
\delta &= \delta_0 + \delta_D(v) - \delta_{\text{Zeeman}}(z) \\
&= \delta_0 + k_{\text{laser}} \cdot v_{\text{atom}} - \frac{\mu_B}{\hbar} \left\{ m_{J,e} g_{J,e} - m_{J,g} g_{J,g} \right\} \cdot B(z) \qquad (4.3) \\
&= 0
\end{aligned}
$$

where the indices e and g denote the excited and ground state, respectively. δ is the overall detuning which determines the scattering force (4.1), and δ_0 denotes the detuning of the slower beam with respect to the transition at zero magnetic field. The different sign of δ_0 and δ_D compared to δ_{Zeeman} comes from the fact that the former two change the laser frequency whereas the latter one alters the resonance frequency. For simplicity, the resonance condition (4.4) is only specified for the case when both the ground state and the excited state are in the Paschen-Back regime. Since our slower operates at magnetic fields on the order of $100\,\text{G}$, this is fullfilled for lithium during the whole slowing process except over a small distance with $B \approx 0$, which is discussed in section 4.4.1

In order to be able to derive an equation for our magnetic field from (4.4), we have to know the equation of motion of an atom. Thus we design our slower for a constant deceleration a during the whole slowing process with a value

$$
a = \zeta \cdot a_{\text{max}},
$$

where the dimensionless factor $0 \leq \zeta \leq 1$ denotes the so-called safety factor. It takes into account for example the finite saturation of the slower beam or imperfections in the magnetic field. The minimal length L_s of the slower is thus in essence determined by ζ and can be calculated to be

$$
L_s = \frac{1}{2\zeta} \cdot \frac{v_{\text{max}}^2 - v_{\text{end}}^2}{a_{\text{max}}},
$$

where v_{max} is the maximal velocity of an atom the slower is still able to cool and v_{end} is the end velocity of the atoms leaving the slower. When inserting the corresponding $v(z)$ into equation (4.4) and solving for $B(z)$, one obtains

$$
\begin{aligned}
B(z) &= B_0 \cdot \sqrt{1 - \frac{z}{L_s}} + B_b & (4.4) \\
B_0 &= \frac{\hbar k_{\text{laser}} \cdot v_{\text{max}}}{\mu_B \cdot \left\{ m_{J,e} g_{J,e} - m_{J,g} g_{J,g} \right\}} & (4.5) \\
B_b &= \frac{\hbar \delta_0}{\mu_B \cdot \left\{ m_{J,e} g_{J,e} - m_{J,g} g_{J,g} \right\}} & (4.6)
\end{aligned}
$$

A common choice is for example the decreasing-field slower with $\delta_0 = 0$ which is depicted in Figure 4.3 (a). The disadvantage of this configuration however is, that the slower beam is in resonance with the trapped atoms in the MOT and thus executes a light pressure onto them or heat up the atoms. Another slower type is the increasing-field slower, depicted in Figure 4.3 (b), with $B_b = -B_0$. In this case, one has a large detuning of the slower beam but also a large magnetic field at the

end of the slower. Since the experimental region is close to the slower end and the magnetic fields can not drop to zero instantaneously, our slower field would therefore disturb the magnetic field of the MOT. Thus in our experiment we use neither of these types but a combination of these two, the so-called spin-flip slower.
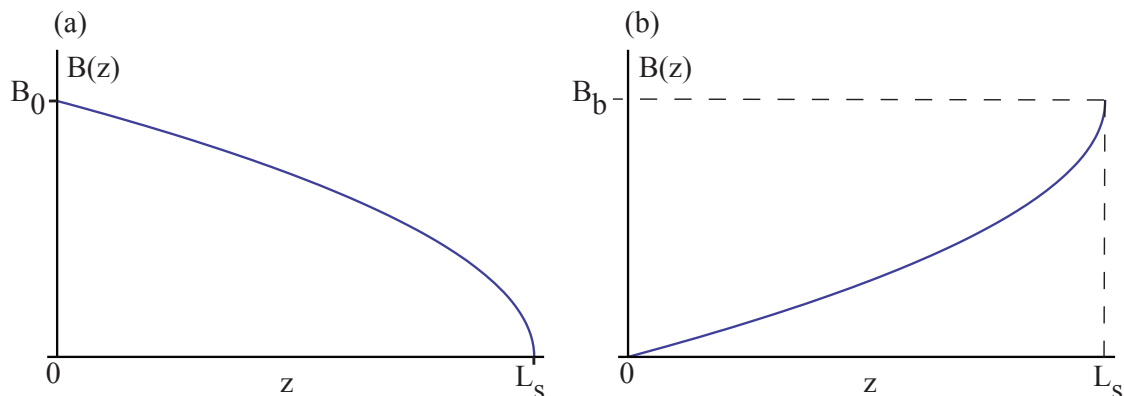
Figure 4.3.: *Characteristics of the magnetic field for a decreasing field slower (a) and an increasing field slower (b)*

4.4. Spin-Flip Slower

The spin-flip slower is a trade-off between a large detuning of the slower beam on the one hand and a low magnetic field near the trapping region on the other hand. The form of the experimentally realised field can be seen in Figure 4.4. Its characterisitic feature is the change of sign in the magnetic field.
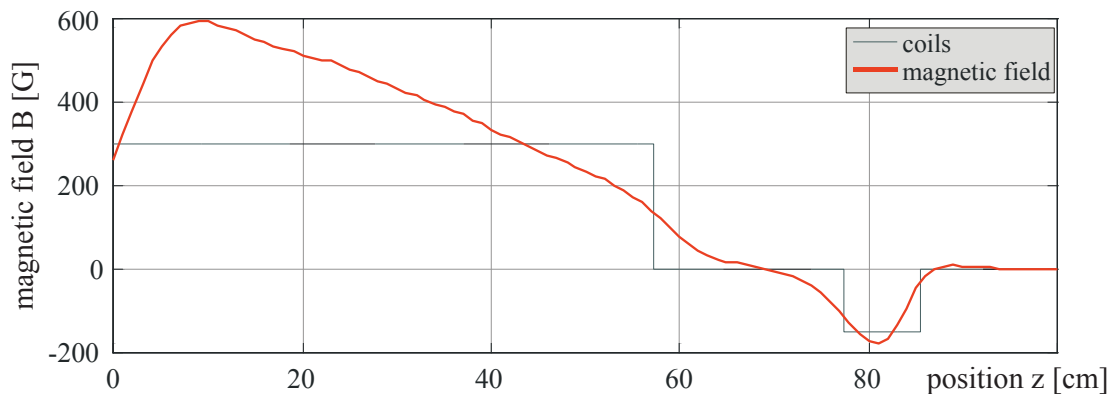
Figure 4.4.: *Numerically calculated magnetic field for our spin-flip slower (modified from [38])*

This feature leads to some experimental difficulties which are explained in 4.4.1. Techniqually, an increasing magnetic field of the form (4.5) can be realised by a coil with spatially varying winding numbers. Since we have a decreasing magnetic field

for $B > 0$ and an increasing magnetic field for $B < 0$, we use two such coils operated with opposite currents.

A schematic of the experimental setup can be seen in Figure 4.1. Atoms leaving the oven, enter the big slower coil which produces the decreasing field. Subesequently they enter the small slower coil and are cooled down to an end velocity of about $30\,\frac{m}{s}$. At the end of the small slower, they drop out of resonance and enter the experimental region where they can be finally trapped. Further theoretical and design considerations for our spin-flip slower can be found in the diploma thesis of Jan Krieger [38]. Note that our slower has been optimised for sodium since it has a larger mass and is thus less effectively cooled (see equation (4.2)).

4.4.1. Cooling processes for lithium

The magnetic field $B(z)$ is almost over the complete length of the slower large enough so that one is in the Paschen-Back regime both for the ground and the excited states. In this case, the energy levels of the magnetic substates are not degenerate anymore and one can adress the excited states of the atoms selectively (see Figure 4.5). The slower beam is chosen to have σ^+-polarisation and a detuning of $\delta_0 = -2\pi \times 300\,\mathrm{MHz}$. For $B > 0$, the cooling transition is then $|2^2 S_{1/2}, m_J = 1/2, m_I = 1\rangle \to |2^2 P_{3/2}, m_J = 3/2, m_I = 1\rangle$. Due to the selection rules introduced in section 2.4, this is a closed transition and one has no losses to other states. For $B < 0$, the atoms see the the slower beam with σ^--polarisation. The closed transition is now $|2^2 S_{1/2}, m_J = -1/2, m_I = -1\rangle \to |2^2 P_{3/2}, m_J = -3/2, m_I = -1\rangle$ and one therefore has to pump the atoms from the $m_F = 3/2$ substate into the $m_F = -3/2$ substate before they enter the small slower. This is done by implementing a distance with small negative magnetic field between the two coils. Because the atoms are then in the Zeeman regime, they are all pumped into $m_F = -3/2$, provided that the time the atoms spent inside this low field region is long enough. To ensure this, a numerical simulation of this pumping process for the case of sodium has been executed [38].

Another thing we have to take into account for $B \approx 0$ is that the quantization axis is not very pronounced. Thus the atoms see both σ^+- and σ^--light. In addition, the magnetic substates are highly degenerate and the level spacing of the excited Hyperfine states is smaller than the natural linwedith Γ. Hence, due to selection rules, atoms can also be excited into the $F = 3/2, 1/2$ states from where they can decay into the lower Hyperfine ground state in which they are lost for further cooling. Thus a second beam, the Repumper, has to be applied which pumps the atoms back into the cooling cycle. As depicted in Figure 4.5, the Repumper, being superimposed with the slower beam, is in resonance with $F = 1/2 \to F' = 3/2$.

4.4.2. Transversal widening of the atomic beam

When the atoms arrive at the end of the small slower, the magnetic field has a maximum and the atoms therefore drop out of resonance, having an end velocity $v_{\mathrm{end}} \approx 30\,\frac{m}{s}$. They subsequently enter the glass cell in which we trap them with our MOT. Until now, we considered only the movement of the atoms in z-direction. But the transversal velocity distribution of the atoms will also widen up during
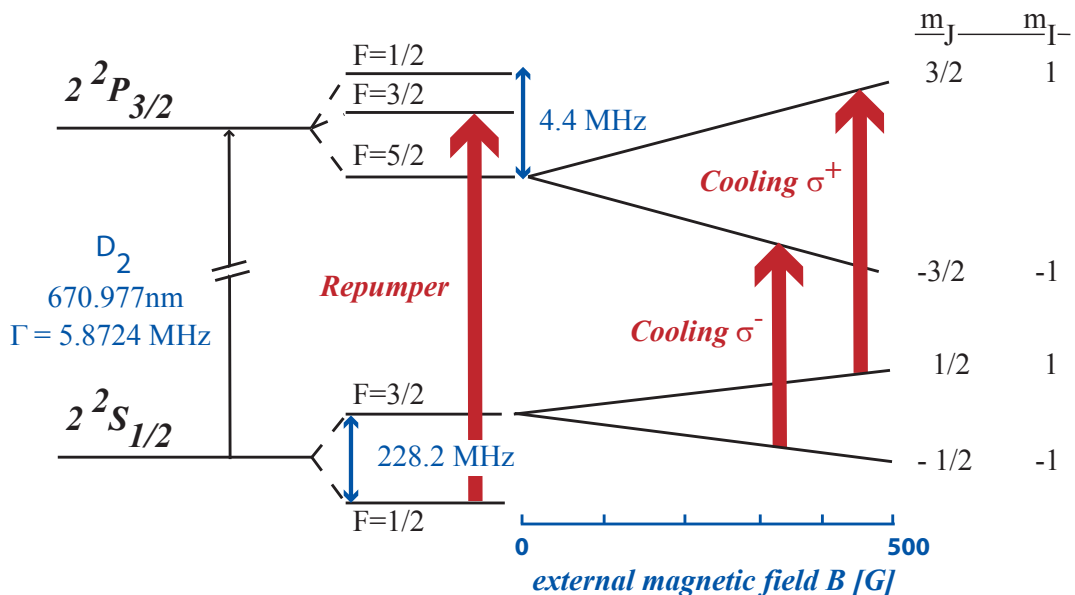
Figure 4.5.: *The relevant transitions for the cooling scheme of lithium. The energy splitting in the Paschen-Back regime is only qualitatively depicted.*

the slowing process. This is caused by spontaneous emission since although the averaged force on the atoms by spontaneous emission is zero, the movement of the atoms due to the recoil momenta of emitted photons can be seen as a *random walk*. The rms-velocity of the atoms in transversal direction depends on the number of scattering processes N and can be calculated to be [44]

$$v_\perp^{\mathrm{rms}} = \frac{\hbar \cdot k_{\mathrm{laser}}}{m_{\mathrm{atom}}} \sqrt{\frac{N}{3}}. \tag{4.7}$$

Inside the Zeeman slower, the longitudinal velocity v_z is large compared to $v_\perp^{\mathrm{rms}}$ which takes at the end average values on the order of $4 \frac{\mathrm{m}}{\mathrm{s}}$. Thus the divergence of the atomic beam due to spontaneous emission is negligible inside the slower. But it plays a crucial role for the loading rate of the MOT. At the end of the slower the divergence Θ of the beam is determined by the ratio

$$\Theta = \frac{2 \cdot v_\perp^{\mathrm{rms}}}{v_{\mathrm{end}}}, \tag{4.8}$$

which is depicted in Figure 4.6.

Since $v_\perp^{\mathrm{rms}}$ depends on the number of scattering processes during the slowing process, the initial velocity v_i of the atoms will determine their divergence. For $v_i = v_{\mathrm{max}} \approx 700 \frac{\mathrm{m}}{\mathrm{s}}$ we have for example about 7000 collisions during the cooling process and thus a divergence of $\Theta = 18°$ which means that the cooled atoms widen up by $3\,\mathrm{mm}$ after a $1\,\mathrm{cm}$ flight distance. Thus when the end velocity of the atoms becomes too small, many of them will not reach the trapping radius of the MOT due to their large divergence (see Figure 4.6). Hence we need a trade-off between a small divergence and a small end velocity which still enables us to effectively trap the atoms in the MOT. The dependency of the loading rate of the MOT on the atoms end velocity is investigated and discussed further in section 5.1.4.
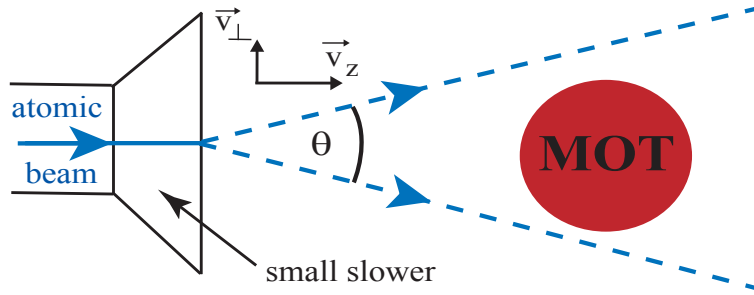
Figure 4.6.: *Divergence of the atomic beam after the small slower.*

4.5. Absorption measurement method

To be able to quantify important characteristics of trapped atom clouds, like for example the total atom number or density distributions, several techniques have been developed over the past decades. For example, one can capture the fluorescence of the atom cloud onto a photodiode and gain information about the total atom number from the signal's strength. Another commonly used technique is the absorption imaging method which can give many insights into the characteristics of the cloud but has the disadvantage that it destroys the cloud.

The main idea of absorption imaging is to probe the trapped atom cloud with a laser pulse. When capturing the transmitted pulse on a CCD camera, the column density $\tilde{n} = \int_{-\infty}^{\infty} \mathrm{d}z \cdot n(\vec{r})$ of the atom cloud can be infered by taking several pictures with and without atoms. From the column density, one can then infer many interesting properties like for example the total atom number N_{atom}, the temperature T_{cloud} or the phase space density of the cloud [45].

A schematic of our experimental implementation is depicted in Figure 4.7. The imaging light is taken from the TA and can be switched on and off with an AOM. When illuminating the atom cloud with the beam, the shadow cast by the atoms in the plane of the cloud is imaged by a lens onto a CCD camera with magnification $M = 0.397$. In general, the absorption of a beam with intensity $I_z(x, y)$ travelling in z-direction through a cloud with density $n(\vec{r})$ and scattering cross section $\sigma(\vec{r})$ is given by the differential equation [31]

$$\frac{\mathrm{d}I_z(x, y)}{\mathrm{d}z} = -\sigma(\vec{r}) \cdot n(\vec{r}) \cdot I_z(x, y), \tag{4.9}$$

where (x, y) denotes the plane of the cloud which is imaged onto the camera. The solution of this differential equation can be quite complicated, since the scattering cross section is dependent on the saturation s_0 of the pulse which itself has a spatial dependence due to the gaussian shape of the beam and also decreases when the pulse pass the cloud due to absorption. But in the specific case when the intensity of the laser pulse $I_0(x, y)$ is much smaller than the saturation intensity I_S, which is the case in our setup, we end up with a constant scattering cross section σ_0 and equation (4.9) simplifies to the Beer equation [46] with the solution

$$I_{\mathrm{absorption}}(x, y) = I_0(x, y) \cdot e^{-\sigma_0 \cdot \tilde{n}(x, y)}, \tag{4.10}$$
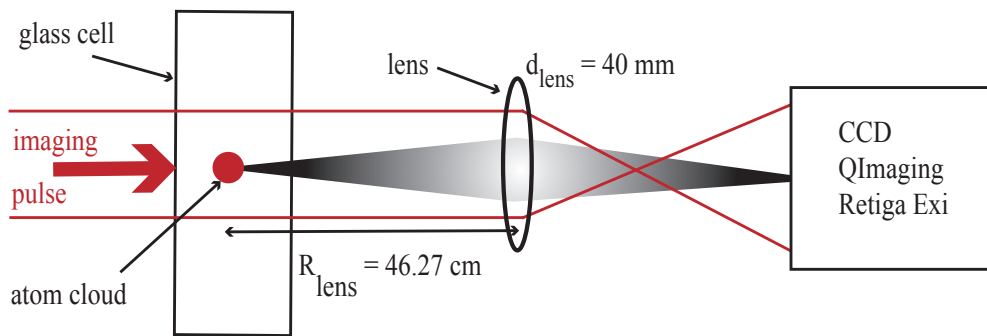
Figure 4.7.: *Setup for absorption imaging. The black rhombus indicates the casted shadow of the atom cloud which is imaged onto the CCD camera. The geometric properties are given for our used setup.*

where $I_{\text{absorption}}(x,y)$ is the intensity of the beam after passing the atom cloud. For $s_0 \ll 1$ the scattering cross section σ_0 for a two level atom at resonance is given by [31]

$$\sigma_0 = \frac{\hbar\omega_0}{2I_S} = \frac{3\lambda^2}{2\pi}. \tag{4.11}$$

For lithium we have to take into account that an excited atom only decays with a probability of $2/3$ into the upper Hyperfine ground state since at $B = 0$ the excited Hyperfine states are not resolved. Thus only two out of three scattered photons are due to absorption of the probe pulse. The scattering cross section for lithium hence modifies to [47]

$$\sigma_{0,\text{Li}} = \frac{\lambda^2}{\pi}.$$

The total atom number can then be obtained from the column density by

$$N_{\text{atom}} = \int\int_{-\infty}^{\infty} \mathrm{d}x \, \mathrm{d}y \, \tilde{n}(x,y) \tag{4.12}$$

$$= -\frac{1}{\sigma_{0,\text{Li}}} \cdot \int\int_{-\infty}^{\infty} \mathrm{d}x \, \mathrm{d}y \, \ln\left(\frac{I_{\text{absorption}}(x,y)}{I_0(x,y)}\right). \tag{4.13}$$

In the experiment, we obtain $I_0(x,y)$ and $I_{\text{absorption}}(x,y)$ by taking three pictures with the CCD camera. The procedure is as follows: First the MOT is loaded till it is saturated. Then, simultaneously, the MOT as well as the slower and atomic beam are turned off and after a certain time of flight t_{TOF} we take the first picture by applying the imaging pulse. This gives us $I_{\text{pic}} = I_{\text{absorption}}(x,y) + B(x,y)$, where $B(x,y)$ is the background noise of the camera. For the second picture we make sure that no atoms are left inside the glasscell[1] before applying the imaging pulse. This reference picture gives us the initial intensity distribution of the laser pulse with additional noise and thus $I_{\text{refpic}} = I_0(x,y) + B(x,y)$. At last we take a picture without any atoms or applying an imaging pulse to get $I_{\text{back}} = B(x,y)$.

---

[1]this is done by including a sufficiently long delay time of about $0.5\,\text{s}$ between the pictures

We can now calculate N_{atom} by using (4.13), but since we measure an averaged value of the intensity for each camera pixel, the integration transforms into a sum over all pixels (i,j) [45]:

$$N_{\text{atom}} = \frac{-1}{\sigma_0} \cdot \frac{A}{M^2} \sum_{\text{pixel } (i,j)} \ln \left(\frac{I_{\text{pic}}(i,j) - I_{\text{back}}(i,j)}{I_{\text{refpic}}(i,j) - I_{\text{back}}(i,j)} \right) \qquad (4.14)$$

where A is the area of each pixel and $\frac{1}{M^2}$ takes the magnification of the atom cloud shadow into account. In our experiment we use a QImaging Retiga Exi camera (without IR filter) with a pixel area of $A = 6.45\,\mu\text{m} \times 6.45\,\mu\text{m}$ and a resolution of 1.4 million pixels. Note that the camera does not measure intensities but only counts the electrons released when absorbing photons. But since we are only interested in relative intensities, this does not play a role for absorption imaging. But when one is interested in the total photon numbers captured with the CCD camera, one would need to multiply the counted electrons by a factor α, which is characteristical for the camera, to obtain the captured photon number. For further details of our imaging procedure one can also refer to [38].

5. Experimental Results

In this chapter, our experimental results are presented. In the first part we characterise the influence of our slower by turning the different experimental knobs our slower provides us with. Our goal is to optimise the loading rate L and the total atom number N_{atom} of our MOT. In the second part we use a CCD camera to calibrate our atom number. This is done by absorption imaging which is explained in section 4.5.

5.1. Characterisation of the Zeeman Slower

For optimisation of the number of trappable atoms, we first investigate how the flux of the atomic beam coming out of the oven depends on the oven temperature. Then we analyse the influence of the slower beam power on the loading rate of the MOT. After this, the current of the big slower coil is scanned since it determines in essence the maximal initial velocity v_{max} of atoms which can still be cooled. At last, we turn the small slower current to see which influence the atoms end velocity has for the amount of trappable atoms. All these measurements are done by collecting the fluorescence signal of the MOT on a photodiode and measure the loading rate and total fluorescence signal.

5.1.1. Oven temperature

The first experimental knob we can turn to improve the loading rate of the MOT is the temperature of our lithium oven. The oven setup is described in section 4.1 and also depicted in Figure 5.1 (a). By heating up the lithium reservoir, the vapour pressure rises and more atoms enter the gas phase. Thus we expect an increase in the loading rate of our MOT for a rising oven temperature. To describe the experimental behaviour we make the following assumptions: Since the atoms pass through a differential pumping stage before entering the Zeeman slower, the pressure p_{slower} in the slower is much smaller than the initial pressure p_{oven} in the oven. The flux of the atomic beam is hence assumed to be [48]

$$\frac{\mathrm{d}M}{\mathrm{d}t} \propto (p_{\mathrm{oven}} - p_{\mathrm{slower}}) \approx p_{\mathrm{oven}}, \tag{5.1}$$

where M is the total atom mass entering the slower.

However, only atoms with a velocity below the maximal initial velocity v_{max} are cooled in the Zeeman slower and thus can be trapped in the MOT. Therefore the MOT loading rate also depends on the velocity distribution $f(v_z)$ which itself is temperature dependent.
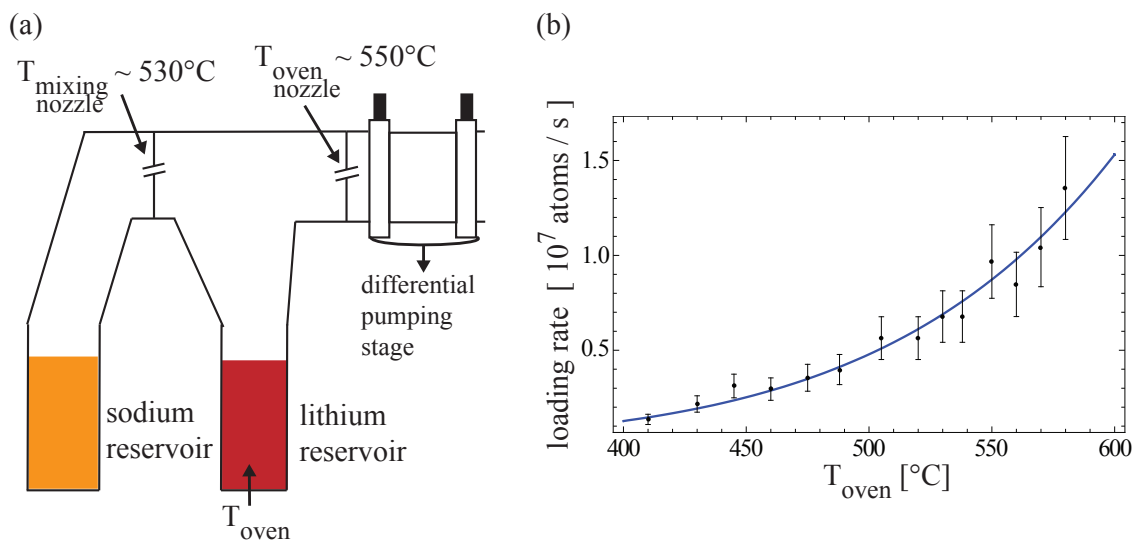
Figure 5.1.: (a): Schematic of our two species oven.
(b): The loading rate of the MOT versus the oven temperature. The blue curve is obtained from our assumed theory.

Inside the oven, the atoms have an isotropic velocity distribution

$$f(v) \propto v^2 \cdot e^{-\frac{m_{\text{Li}} \cdot v^2}{2 \cdot k_B \cdot T}}, \tag{5.2}$$

where m_{Li} is the lithium mass, k_B is the boltzmann factor and T is the temperature of the gas. The probability of an atom to pass the oven nozzle is proportional to v [34] and thus to obtain the distribution behind the oven nozzle, the former $f(v)$ is multiplied by v which leads to a velocity distribution in the z-direction when entering the Zeeman slower of [48]

$$f(v_z) \propto v_z^3 \cdot e^{\left(-\frac{m_{\text{Li}} \cdot v_z^2}{2 \cdot k_B \cdot T}\right)}. \tag{5.3}$$

Hence, we expect our MOT loading rate L to be [49]

$$L \propto p_{\text{oven}}(T) \cdot \frac{\int_0^{v_{\text{max}}} \mathrm{d}v_z \; v_z^3 \cdot e^{\left(-\frac{m_{\text{Li}} \cdot v_z^2}{2 \cdot k_B \cdot T}\right)}}{\int_0^\infty \mathrm{d}v_z \; v_z^3 \cdot e^{\left(-\frac{m_{\text{Li}} \cdot v_z^2}{2 \cdot k_B \cdot T}\right)}}. \tag{5.4}$$

But since the gaseous lithium will collide with the walls of the vacuum chamber, which is not on the oven temperature, the gas temperature when passing the oven nozzle will not coincide with T_{oven}. Therefore we assume the gas temperature to be a mixture of the oven temperature T_{oven} and the temperature of the vaccum chamber T_{chamber}

$$T_{\text{gas}} = \beta \cdot T_{\text{oven}} + (1 - \beta) \cdot T_{\text{chamber}},$$

where β is a dimensionless constant with $0 \leq \beta \leq 1$.

We assume that T_{chamber} itself does not depend on T_{oven}, which is justified due to the finite heat conduction of the vacuum chamber and the spatial separation

between the oven oven and the vacuum chamber. For our fitting procedure we assume $T_{\text{chamber}} = 540\,°\text{C}$, which is the mean of the oven nozzle and mixing nozzle temperature (see Figure 5.1 (a)). Our result is displayed in Figure 5.1 (b), where the dependency of the vapour pressure from the temperature is taken from [30] and $\beta \approx 0.5$ is the fitting result. One can see that the fit agrees well with our data within the error bars. In addition, $\beta = 0.5$ seems quite reasonable since one obtains then simply an equilibrium between both temperatures,

$$T_{\text{gas}} = \frac{T_{\text{oven}} + T_{\text{chamber}}}{2}.$$

In conclusion, we observe that a higher oven temperature leads to larger loading rates of the MOT. But we are limited with the temperature to about $600\,°\text{C}$, since for higher temperatures the aluminium, which is wrapped around the vacuum chamber to enhance the heating efficiency, would melt. In addition, higher temperatures would also limit the working time of our lithium reservoir.

5.1.2. Slower beam power

From equation (4.1) it follows that the scattering rate depends on the saturation s_0 of the slower beam. Thus when decreasing the power in the slower beam[1], s_0 becomes smaller and the scattering force on the atoms decreases. Since a_{max} saturates with increasing intensity, we expect less trappable atoms leaving the slower when decreasing the slower power below a critical value. This behaviour is experimentally verified for different detunings δ_0 of the slower beam. In Figure 5.2 the behaviour is
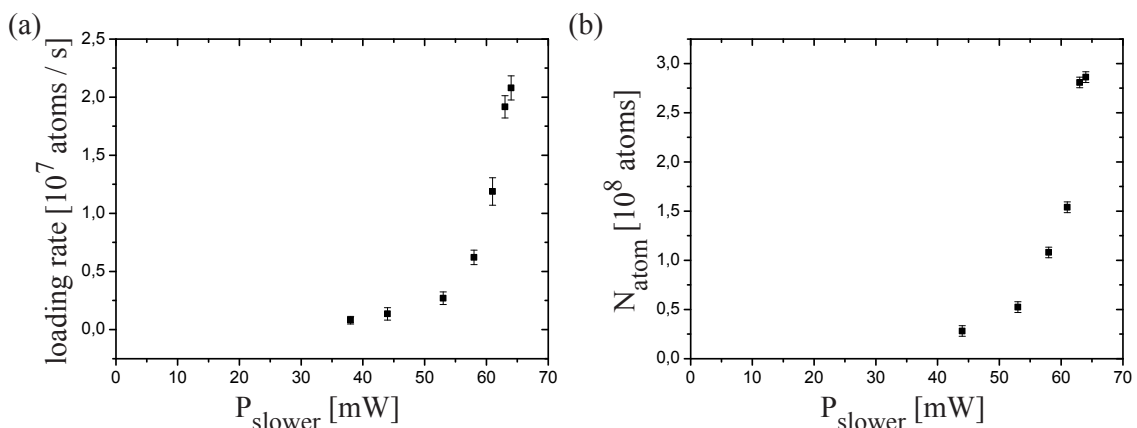
Figure 5.2.: *(a): loading rate L versus slower beam power P_{slower}.*
(b): atom number N_{atom} versus slower beam power P_{slower}.

only shown for $\delta_0 = -2\pi \times 300\,\text{MHz}$ since the characteristics have been the same for all measurements. The overall slower power P_{slower} is measured including the repumper beam with a ratio of

$$\frac{P_{\text{slower}} - P_{\text{rep}}}{P_{\text{rep}}} = 2.5,$$

---

[1]this can be done with the VCO level of the acousto-otic modulator (AOM)

where P_{rep} is the power of the repumper beam.

One can see that both the loading rate L and the total atom number N_{atom} have a very steep slope above a beam power of $50\,\text{mW}$. This can be seen as an evidence that we are limited by our beam power. But with the current setup we are not able to put more power into the slower beam since this comes at the cost of less power in the z-beams of the MOT which would also reduce the loading rate.

A possible explanation for this behaviour is the intensity profile of the beam. The saturation s_0 is spatially dependent and we assume the intensity of the beam to have a gaussian profile as a rough approximation. When now reducing the power, the peak intensity decreases and the radius r of the beam with $s_0 \geq 1$ becomes smaller which is depicted in Figure 5.3 (a). Thus on the wings of the beam where $s_0 < 1$, the atoms, especially the ones with a large divergence at the end of the slower, are not effectively cooled and hence the loading rate decreases. To investigate this behaviour further, one could put an adjustable iris into the beam path. Thereby one can cut off the wings of the beam at a constant peak intensity and observe the influence on the loading rate (see Figure 5.3 (b)). If the loading rate shows a similar behaviour as for reducing the slower power, this would be an evidence that the saturation at the sides is not sufficient for smaller slower powers.
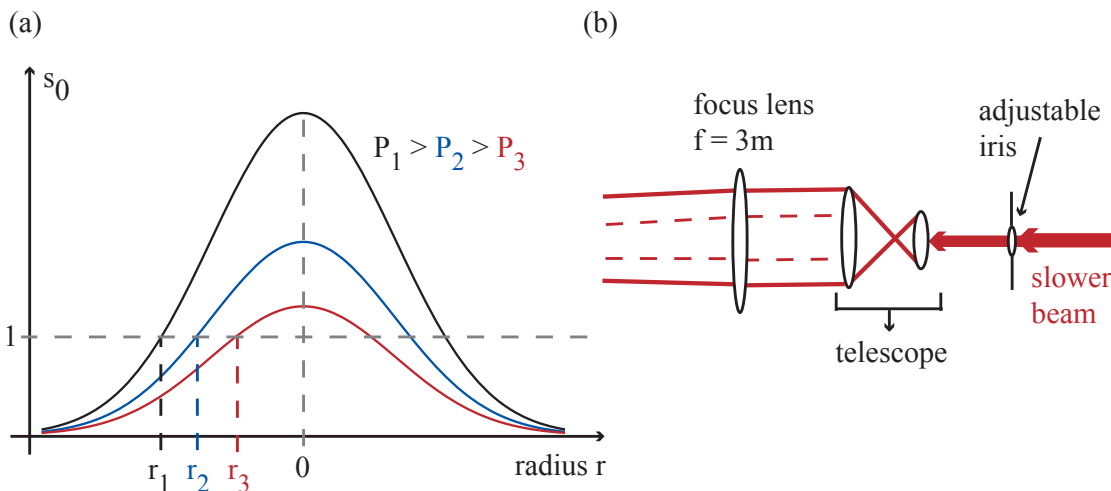
Figure 5.3.: (a): Intensity profile for different slower powers. The widths with $s_0 \geq 1$ are indicated.
(b): Scheme of the proposal experiment to test our hypothesis.

Another possible way to increase the loading rate could be to use a different telescope to widen up the slower beam. If the slower beam is too small to completely overlap with the atomic beam, we are limited in the amount of trappable atoms. Thus this should be checked since it could increase our loading rate without much effort.

If it proves true at the end that we are only limited by our power, one could still consider to seed a Tapered Amplifier (TA) with the slower beam and thus get much higher powers. But this would be a rather expensive solution and is not considered at the moment.

5.1.3. Big slower current

After increasing the flux of the atomic beam from the oven and optimising the shape of the slower beam by a telescope, we now map out the influence of the big slower parameter, namely the current I_{bs}. The atoms entering the slower have a velocity distribution $f(v_z)$, which in combination with the maximal coolable initial velocity v_{max} determines the amount of trappable atoms. Thus, we expect the loading rate of our MOT to be proportional to

$$L \propto \int_0^{v_{\mathrm{max}}} \mathrm{d}v_z \; v_z^3 \cdot e^{\left(-\frac{m_{\mathrm{Li}} \cdot v_z^2}{2 \cdot k_B \cdot T}\right)}, \tag{5.5}$$

where we assumed the same velocity distribution in section 5.1.1.

As can be seen from equation (4.6), v_{max} depends linearly on B_0. We operate our lithium oven at $550\,°\mathrm{C}$ and thus, according to equation (5.3), the most likely velocity would be at about $1800\,\frac{\mathrm{m}}{\mathrm{s}}$. Since in our experiment v_{max} is on the order of $700\,\frac{\mathrm{m}}{\mathrm{s}}$, we expect a steep slope for increasing B_0, which is in essence determined by the magnetic field of the big slower and the detuning δ_0 of the slower beam. The result of our measurement is shown in Figure 5.4.
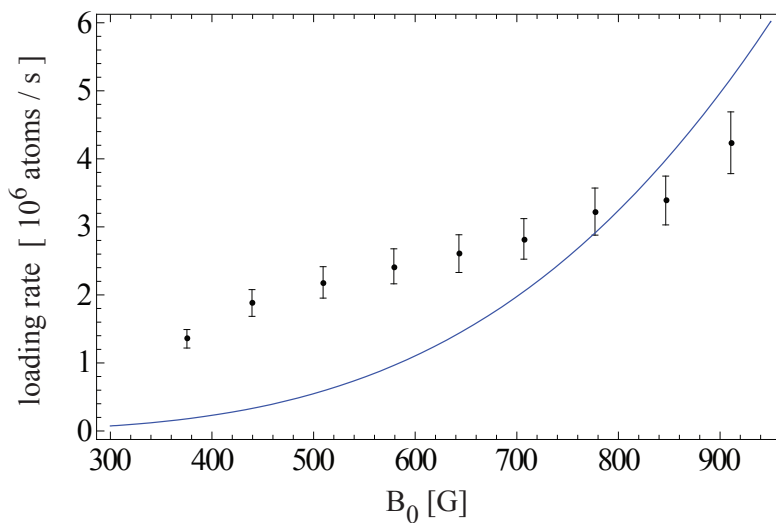
Figure 5.4.: *Loading rate of the MOT versus B_0: the blue curve is obtained from theory.*

With our measurement, we can confirm that a larger v_{max} enhances the loading rate of our MOT, but the slope is not as steep as we would expect from our theory. This deviation is probably caused by the divergence of the atoms at the end of the small slower due to scattering, which is explained in section 4.4.2. Atoms with higher initial velocity perform more scattering processes during the cooling and therefore have a larger divergence when leaving the Zeeman slower. For example an atom entering the Zeeman slower with $v = 400\,\frac{\mathrm{m}}{\mathrm{s}}$ has a divergence of $14\,°$ whereas an atom entering with $v = 800\,\frac{\mathrm{m}}{\mathrm{s}}$ has a divergence of about $19\,°$. Thus when increasing the magnetic field of the big slower and therefore v_{max}, many of the atoms whose velocity

is now below $v_{\max}$ can still not be trapped. The resulting increase in the loading rate for enlarged $v_{\max}$ is hence smaller than predicted by our theory.

Another reason one could think of is that by increasing the magnetic field B_0, the gradient of the magnetic field also is increased. Thus initial fast atoms could drop out of resonance and would thus be lost to cooling, which would also explain the lower loading rate compared to theory. But we exclude this for our setup since the Zeeman slower has been optimized for sodium, whose mass is about four times larger and hence the deceleration for lithium atoms is more than sufficient.

In conclusion, we see that it is advantageous for our loading rate to operate our big slower at high currents. However, above $I_{bs} \approx 26\,\mathrm{A}$, the power dissipated in the slower coils leads for continuous operation to a too high coil temperature. An idea is hence to pulse the slower during the lithium MOT loading phase to higher currents and thus have an averaged power which the water cooling of the slower coil can compensate.

5.1.4. Small slower current

For this measurement, the oven temperature was set to $T_{oven} = 550\,°\mathrm{C}$, the big slower current to $I_{bs} = 16\,\mathrm{A}$ and the detuning to $\delta_0 = -2\pi \times 300\,\mathrm{MHz}$. Our results are shown in Figure 5.5. For currents below $6.5\,\mathrm{A}$, the magnetic field at the slower end
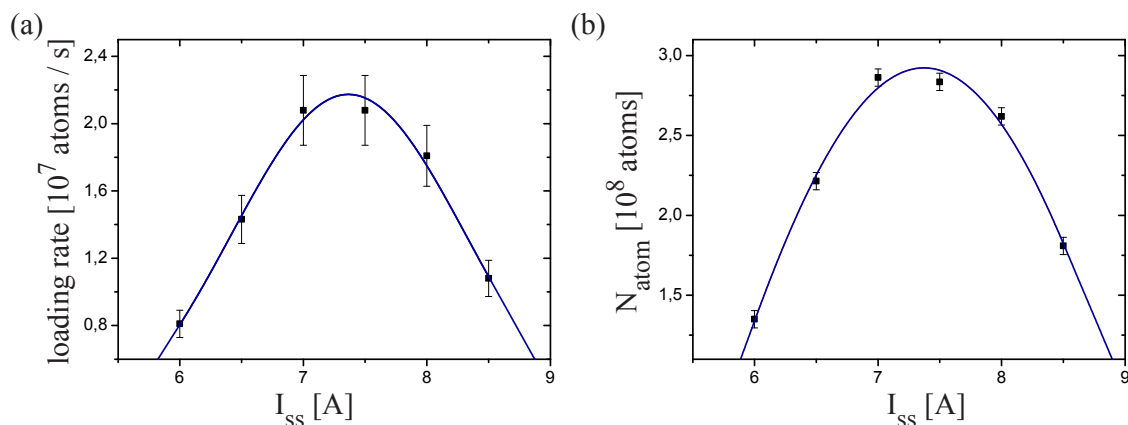
Figure 5.5.: *(a): loading rate L versus small slower current I_{ss}*
(b): atom number N_{atom} versus small slower current I_{ss}
In both cases a gaussian fit (blue line) is fitted as a guide to the eye.

is small and thus the end velocity v_{end} of the atoms is quite high. A large amount of the atoms then exceeds the maximal trapping velocity v_{trap} of the MOT and both the loading rate L and the total atom number N_{atom} are rather small. As we increase the current, v_{end} becomes smaller and both L and N_{atom} rises until they reach their maximum. This can be explained by the fact that the end velocity v_{end} is then smaller than the trapping velocity v_{trap} and thus a further increase in I_{ss} has no positive effect on the number of trappable atoms. Instead, when increasing I_{ss} even further, L and N_{atom} begin to drop again. This has two reasons. First, when v_{end} becomes smaller, the divergence of the atoms leaving the Zeeman slower rises (see

4.4.2) and thus less atoms can arrive within the trapping radius of the MOT. Second, for large I_{ss} the atoms can be even accelerated back into the slower and less atoms reach the trapping radius of the MOT at all. In our measurement we can not say with certainty which of these two effects causes the dropping of our loading rate. To check this, one could use the iris method from section 5.1.2. When cutting off the beam at the wings and observing no change in the loading rate, this could be seen as an evidence that the atoms are accelerated back into the slower.

To obtain an estimated FWHM of the plateau, we use a gaussian fit without being theoretically motivated. The loading rate has its maximum at about $I_{ss_{max}} = 7.4\,\text{A}$ and a FWHM of $\Delta I_{ss} \approx 2.2\,\text{A}$.

These numbers are important for the simultaneous loading of a sodium and lithium MOT. In the experiment, sodium is loaded optimally at $I_{ss} = 9\,\text{A}$ and therefore we will still have a loading rate for lithium of about $25\,\%$ of the peak value when loading sodium. Thus the lifetime of the lithium MOT during the sodium loading is enhanced by a factor $4/3$, where we have not considered the influence of the sodium MOT for the lifetime of the lithium MOT yet [50].

In addition, we carefully checked this behaviour for different detunings δ_0 of our slower beam but found out that for $\delta_0 = -2\pi \times 300\,\text{MHz}$ our MOT is optimised.

5.2. Atom number calibration using absorption imaging

As mentioned before, to optimise our MOT, we capture its fluorescence onto a photodiode and derive the total atom number from the signal's strength. But this method suffers from the uncertainty in the determination of the captured solid angle and the scattering rate and the measured atom numbes are therefore not exact. Hence we also use a more sophisticated method to quantify our trapped atom numbers, namely absorption imaging which was introduced in section 4.5.

After turning off the MOT we image our atoms with a time delay of t_{TOF}. To be on resonance during the imaging pulse, we have to shift the frequency of the TA. Since this frequency shift is not instantaneous [36], we measure how the chosen time of flight t_{TOF} influences our measured atom number N_{atom}. Therefore we scan t_{TOF} in steps of $0.2\,\text{ms}$ from $t_{\text{TOF}} = 0.1\,\text{ms}$ up to $t_{\text{TOF}} = 1.9\,\text{ms}$ and take for every t_{TOF} three shots. Figure 5.6 displays the result: Each point represents the mean value of the three measurements with the standard deviation of the mean as error. For small time of flights, the three measurements show a large variance. This can be due to the fact that the frequency shift of the TA takes up to $1\,\text{ms}$ with possible oscillations and thus the detuning of the imaging pulse can differ from zero. For $t_{\text{TOF}} > 0.7\,\text{ms}$ the atom number is almost constant and thus gives us a reliable result for our atom number calibration. We therefore choose $t_{\text{TOF}} = 0.8\,\text{ms}$ and take ten shots of the MOT. After averaging, we obtain

$$N_{\text{atom}} = (2.68 \pm 0.67) \times 10^8 \text{ atoms.}$$

In comparison, we obtain an atom number of $(1.81 \pm 0.09) \times 10^8$ atoms with the fluorescence signal on the photodiode. Thus our fluorescence measurement just gives

an approximation of the total atom number and differs from the one obtained by absorption imaging by about 30 %.
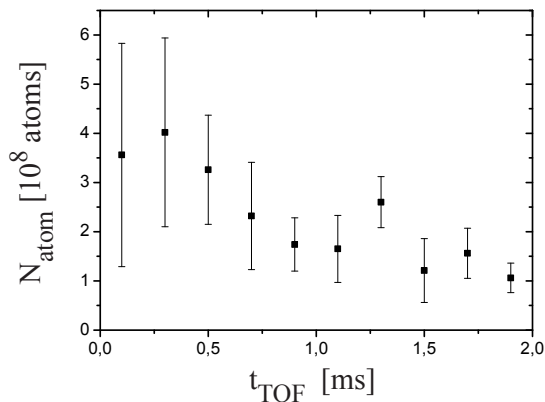
Figure 5.6.: *Total atom number N_{atom} versus time of flight t_{TOF}.*

When imaging the atom cloud, we choose a rather long imaging duration. Thus during the imaging process, the atoms experience a recoil and drop out of resonance due to the Doppler effect. Hence, the absorbtion of the pulse decreases which leads to an underestimation our total atom number according to equation (4.14). Our atom number calibration with absorption imaging gives us therefore at least a lower bound for our total atom number.

The total atom numbers of the MOT after the optimisation of all experimentally tunable paramters are given in Table 5.1. In conclusion, absorption imaging is our first choice when measuring the total atom number. To optimise the MOT however, the fluorescence measurement with a photodiode is the method of our choice since it has a 'live' character and is non-destructive.

Method	Total atom number [10^8 atoms]
fluorescence on photodiode	2.7 ± 0.4
absorption imaging	4.0 ± 1.0

Table 5.1.: *Final results for the total atom number after all optimisation steps.*

Note that the time of flight method can also be used to obtain the temperature of our MOT. Therefore one assumes a gaussian density distribution inside the MOT and determines the $^1/_e$-radius[2] of the cloud for different t_{TOF}. The $^1/_e$-radius behaves as [47]

$$r_{^1/_e}\left(t_{TOF}\right) = \sqrt{r_{^1/_e}^2\left(t=0\right)^2 + \frac{2k_B T}{m_{Li}} \cdot \left(t_{TOF}\right)^2},$$

where $t = 0$ defines the time the MOT is turned off. Thus the temperature of our MOT can be obtained by a time of flight series and a subsequent fit. However, later on when sympathetically cooling our lithium with the sodium in the magnetic trap,

---

[2]radius for which the density dropped to $^1/_e$ of its peak value

our achievable end temperature will first and foremost depend on the size and the temperature of the sodium MOT and thus we are not constrained by the temperature of our lithium MOT .

6. Conclusion and Outlook

In the course of this thesis, we were able to trap a cloud of lithium atoms in a magneto-optical trap which is another milestone on our way towards our desired bose-fermi mixture. First we built up a lasersystem for lithium consisting of a master laser with stable frequency and low output power and a slave laser with high output power being beat-locked onto the master laser. The frequency stabilisation of the master laser, a grating stabilized diode laser, has been achieved by setting up doppler-free saturation spectroscopy for lithium and locking the laser onto the crossover peak of the spectroscopy. With our setup, we reached a stability of about 1 MHz, which is more than sufficient for laser cooling.

This laser system enabled us finally to cool lithium atoms and trap them in our MOT, as to be seen in Figure 6.1. Since the trapped cloud was rather small at the beginning, we optimized it using all the experimental knobs our setup provided us with. In particular, we investigated the dependency of the MOT properties from the oven temperature, the currents through the Zeeman slower coils and the shape of the slower beam. In addition, the behaviour for different power splittings in our beams or the detuning has also been checked. Finally we were able to optimize our MOT to have an atom number of about 4×10^8 atoms with more than half of the atoms being loaded in less than 10 s.
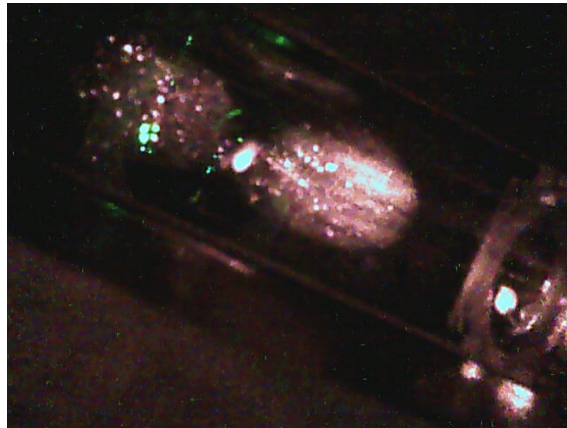
Figure 6.1.: *First picture of our MOT*

The next step towards our experimental goal of investigating polarons is to load the lithium atoms from the MOT into a magnetic trap since the temperatures achievable in a MOT are not sufficient to cool the atoms into quantum degeneracy. The temperatue limit in the MOT is given by the light scattering and hence another cooling technique has to be used. In the magnetic trap, the atoms are cooled by microwave induced evaporation of sodium. Hot sodiums are removed from the trap

and the remaining cooler ones thermalizes by inter and intra species collisions and thus the temperature is decreased at the cost of loosing sodium atoms. The transfer into a magnetic trap has already been achieved for sodium and thus we can rely on an existing trap setup. Additionally, evaporative cooling for sodium alone has also been performed and a sodium condensate achieved. Thus a next step will be to control the evaporative cooling in the presence of lithium atoms. As mentioned in the introduction, for our polaron experiment we need to control the interactions between both species using Feshbach resonances. Hence we need the magnetic field as a free parameter and trapping atoms inside an optical dipole trap (ODT) becomes essential. The transfer from the magnetic trap into our dipole trap [51] has been done for sodium already. Therefore we are optimistic to see intra species Feshbach resonances of sodium in the near future. After all this is done, we can finally focus on the inter species Feshbach resonances between sodium and lithium.

With our current setup we are not limited to the investigation of polarons, but we could also use the sodium only as a 'refrigerator' for lithium and thus produce large degenerate fermionic clouds by evaporating the complete sodium out of the trap. Thus we could produce large spin mixtures of the $|2^2 S_{1/2}, F = 1/2\rangle$ substates, which has a broad Feshbach resonance at $834\,\mathrm{G}$ with a width of $300\,\mathrm{G}$ [52]. The properties of purely fermionic systems, like for example the compressibility of an ideal Fermi gas [53], the superfluidity of a strongly interacting Fermi gas [54] or fermi polarons in an imbalanced spin mixture [55, 56] has been of great interest in recent years. Another result has been for example the verification of universal relations, the Tan relations [57, 58, 59], in the unitarity regime [60] which can give new insights in the many-body physics of these systems. However, there are still a lot of unsolved questions and hence the physics of fermionic systems will remain a challenging and interesting field in the years to come.

In conclusion, the near future at the NaLi experiment promises to be really exciting.

A. Properties of Lithium

The following data and graphs are taken from [30] and characterize the D_2-line of ^{6}Li.

Item	Notation	Value
mass	m_{Li}	$9.9883414 \times 10^{-27}\,\text{kg}$
nuclear spin	I_{Li}	1
wavelength	λ	$670.977338\,\text{nm}$
frequency	ν	$446.799677\,\text{THz}$
lifetime	τ	$27.102\,\text{ns}$
natural linewidth	Γ	$2\pi \times 5.8724\,\text{MHz}$
atomic recoil velocity	v_{rec}	$9.886776\,\frac{\text{cm}}{\text{s}}$
recoil temperature	T_{rec}	$3.53581152\,\mu\text{K}$
saturation intensity	I_S	$2.54\,\frac{\text{mW}}{\text{cm}^2}$
total electronic g-factor ground state	$g_J(2^2S_{1/2})$	2.0023010
total electronic g-factor excited state	$g_J(2^2P_{3/2})$	1.335
g-factor of the nucleus	g_I	-0.0004476540
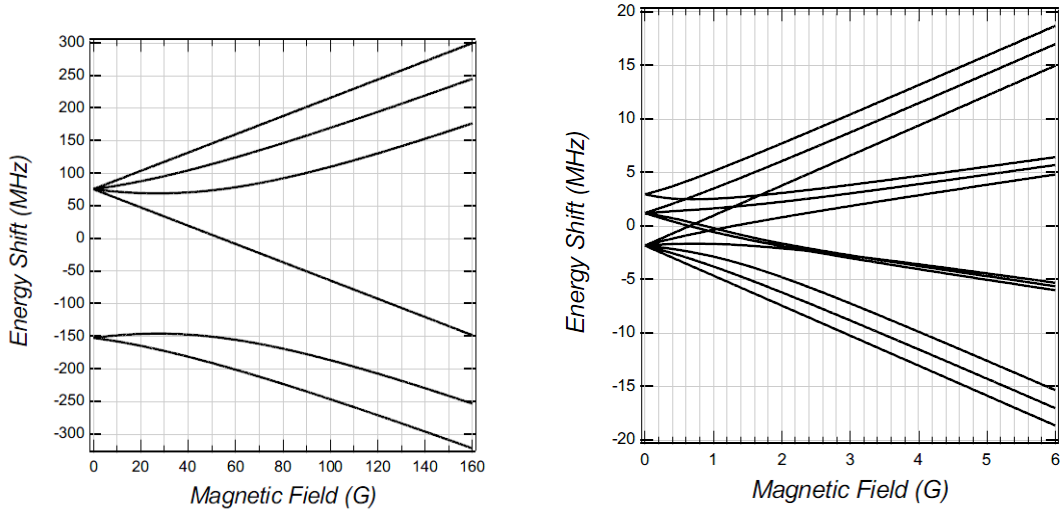
Figure A.1.: *magnetic field dependence for the $2^2S_{1/2}$ state (left) and the $2^2P_{3/2}$ state (right)*

Bibliography

[1] W. Gerlach and O. Stern. Der experimentelle Nachweis der Richtungsquantelung im Magnetfeld. *Zeitschrift für Physik A Hadrons and Nuclei*, **9**(1):349–352, 1922.

[2] P.A.M. Dirac. The Quantum Theory of the Electron. *Proceedings of the Royal Society of London. Series A, Containing Papers of a Mathematical and Physical Character*, **117**(778):610–624, 1928.

[3] P.A.M Dirac. Dirac: The Quantum Theory of the Electron II. In *Proc. Roy. Soc. London A*, volume 118, pages 351–361, 1928.

[4] TH Maiman. Stimulated optical radiation in ruby. *Nature*, **187**:493–494, 1960.

[5] S.N. Bose. Plancks Gesetz und Lichtquantenhypothese. *Z. Phys.*, **24**:178, 1924.

[6] A. Einstein. Quantentheorie des einatomigen idealen Gases. *Sitzungsberichte der Königlich-Preußischen Akademie der Wissenschaften*, **1**:3, 1925.

[7] W.D. Phillips and H. Metcalf. Laser deceleration of an atomic beam. *Physical Review Letters*, **48**(9):596–599, 1982.

[8] S. Chu, L. Hollberg, JE Bjorkholm, A. Cable, and A. Ashkin. Three-Dimensional Viscous Confinement and Cooling of Atoms by Resonance Radiation Pressure. *Physical Review Letters*, **55**(1):48–51, 1985.

[9] EL Raab, M. Prentiss, A. Cable, S. Chu, and DE Pritchard. Trapping of Neutral Sodium Atoms with Radiation Pressure. *Physical Review Letters*, **59**(23):2631–2634, 1987.

[10] M.H. Anderson, J.R. Ensher, M.R. Matthews, C.E. Wieman, and E.A. Cornell. Observation of Bose-Einstein Condensation in a Dilute Atomic Vapor. *science*, **269**(5221):198, 1995.

[11] KB Davis, M.O. Mewes, MR Andrews, NJ Van Druten, DS Durfee, DM Kurn, and W. Ketterle. Bose-Einstein Condensation in a Gas of Sodium Atoms. *Physical Review Letters*, **75**(22):3969–3973, 1995.

[12] MR Andrews, CG Townsend, H.J. Miesner, DS Durfee, DM Kurn, and W. Ketterle. Observation of Interference Between Two Bose Condensates. *Science*, **275**(5300):637, 1997.

[13] M. Albiez, R. Gati, J. Fölling, S. Hunsmann, M. Cristiani, and M.K. Oberthaler. Direct observation of tunneling and nonlinear self-trapping in a single bosonic Josephson junction. *Physical review letters*, **95**(1):10402, 2005.

[14] S. Inouye, MR Andrews, J. Stenger, H.J. Miesner, DM Stamper-Kurn, and W. Ketterle. Observation of Feshbach resonances in a Bose–Einstein condensate. *Nature*, **392**(6672):151–154, 1998.

[15] B. DeMarco and DS Jin. Onset of Fermi Degeneracy in a Trapped Atomic Gas. *Science*, **285**(5434):1703, 1999.

[16] J. Bardeen, LN Cooper, and JR Schrieffer. Microscopic Theory of Superconductivity. *Physical Review*, **106**(1):162–164, 1957.

[17] MW Zwierlein, JR Abo-Shaeer, A. Schirotzek, CH Schunck, and W. Ketterle. Vortices and superfluidity in a strongly interacting Fermi gas. *Nature*, **435**(7045):1047–1051, 2005.

[18] C.A. Regal, C. Ticknor, J.L. Bohn, and D.S. Jin. Creation of ultracold molecules from a Fermi gas of atoms. *Nature*, **424**(6944):47–50, 2003.

[19] S. Jochim, M. Bartenstein, A. Altmeyer, G. Hendl, S. Riedl, C. Chin, J. Hecker Denschlag, and R. Grimm. Bose-Einstein Condensation of Molecules. *Science*, **302**(5653):2101, 2003.

[20] MW Zwierlein, CA Stan, CH Schunck, SMF Raupach, S. Gupta, Z. Hadzibabic, and W. Ketterle. Observation of Bose-Einstein condensation of molecules. *Physical review letters*, **91**(25):250401, 2003.

[21] M. Greiner, C.A. Regal, and D.S. Jin. Emergence of a molecular Bose–Einstein condensate from a Fermi gas. *Nature*, **426**(6966):537–540, 2003.

[22] L.P. Pitaevskiĭ and S. Stringari. Bose-Einstein Condensation. Oxford University Press, USA, 2003.

[23] J. Tempere, W. Casteels, MK Oberthaler, S. Knoop, E. Timmermans, and JT Devreese. Feynman path-integral treatment of the BEC-impurity polaron. *Physical Review B*, **80**(18):184504, 2009.

[24] J. Appmeier. Immersed Quantum Systems: A Sodium Bose-Einstein Condensate for Polaron Studies. PHD thesis, Universität Heidelberg, 2010.

[25] W. Demtröder. Experimentalphysik 3 - Atome, Moleküle und Festkörper, volume 3,überarbeitete Auflage. Springer, 2005.

[26] I. Hertel and CP Schulz. Atome, Moleküle und optische Physik 1: Atomphysik und Grundlagen der Spektroskopie. Springer-Lehrbuch. Springer Verlag, Berlin, 2007.

[27] H-M. Meyer and T. Schmidutz. F65: Electromagnetically induced transparency. Miniscience project, Universität Heidelberg, 2008.

[28] P. Zeeman. The effect of magnetisation on the nature of light emitted by a substance. *Nature*, **55**(1424):347, 1897.

[29] J. Vanier and C. Audoin. The quantum physics of atomic frequency standards. Hilger, 1989.

[30] M.E. Gehm. Properties of 6Li. *The current version of the document is available at http://www. phy. duke. edu/research/photon/qoptics/techdocs*, **58**, 2003.

[31] H. J. Metcalf and P. van der Straten. Laser Cooling and Trapping. Springer-Verlag, 2002.

[32] L. Ricci, M. Weidemüller, T. Esslinger, A. Hemmerich, C. Zimmermann, V. Vuletic, W. König, and T. W. Hänsch. A compact grating-stabilized diode laser system for atomic physics. *Optics Communications*, **117**(5-6):541–549, June 1995.

[33] V. Volchkov. Cold Lithium Atoms For Future Polaron Experiments. Diploma thesis, Universität Heidelberg, 2009.

[34] W. Demtröder. Laserspektroskopie, volume 5. Springer, 2007.

[35] B. E. A. Saleh and M. C. Teich. Photonics, volume 2. Wiley, 2007.

[36] A. Bergschneider. Studies of Lithium Atoms in a Magneto-Optical Trap. Bachelor thesis, Universität Heidelberg, 2010.

[37] M. Repp. Aufbau einer Vakuumapparatur für Experimente mit ultrakalten fermionischen und bosonischen Quantengasen. Diploma thesis, Universität Heidelberg, 2007.

[38] J. Krieger. Zeeman-Slower und Experimentsteuerung für das NaLi-Experiment. Diploma thesis, Universität Heidelberg, 2008.

[39] J.V. Prodan and W.D. Phillips. Chirping the light–fantastic? Recent NBS atom cooling experiments. *Progress in Quantum Electronics*, **8**(3-4):231–235, 1984.

[40] L. Moi. Application of a very long cavity laser to atom slowing down and optical pumping. *Optics Communications*, **50**(6):349–352, 1984.

[41] M. Zhu, CW Oates, and JL Hall. Continuous High-Flux Monovelocity Atomic Beam Based on a Broadband Laser-Cooling Technique. *Physical review letters*, **67**(1):46–49, 1991.

[42] W. Ketterle, A. Martin, M.A. Joffe, and D.E. Pritchard. Slowing and Cooling Atoms in Isotropic Laser Light. *Physical review letters*, **69**(17):2483–2486, 1992.

[43] R. Gaggl, L. Windholz, C. Umfer, and C. Neureiter. Laser cooling of a sodium atomic beam using the Stark effect. *Physical Review A*, **49**(2):1119–1121, 1994.

[44] M.A. Joffe, W. Ketterle, A. Martin, and D.E. Pritchard. Transverse cooling and deflection of an atomic beam inside a Zeeman slower. *Journal of the Optical Society of America B*, **10**(12):2257–2262, 1993.

[45] W. Ketterle, DS Durfee, and DM Stamper-Kurn. Making, probing and understanding Bose-Einstein condensates. In *Proceedings of the International School of Physics-Enrico Fermi*, page 67, 1999.

[46] Wolfgang Demtröder. Experimental Physik 2, volume 4. Springer, 2006.

[47] M. Zwierlein. Cooling and Trapping a Bose-Fermi Mixture of Dilut Atomic Gases. Diploma thesis, Massachusetts Institute of Technology, 2001.

[48] Wolfgang Demtröder. Experimental Physik 1. *Springer*, 2006.

[49] K.J. Günter. Design and implementation of a Zeeman slower for 87Rb. *Report, Ecole Normale Supérieur, Paris*, 2004.

[50] Z. Hadzibabic. Studies of a Quantum Degenerate Fermionic Lithium Gas. PHD thesis, Massachusetts Institute of Technology, 2003.

[51] Raphael Scelle. Cooling, Plugging, Trapping: Exploiting Optical Dipole Potentials For Polaron Experiments. Diploma thesis, Universität Heidelberg, 2009.

[52] M. Bartenstein, A. Altmeyer, S. Riedl, R. Geursen, S. Jochim, C. Chin, J.H. Denschlag, R. Grimm, A. Simoni, E. Tiesinga, et al. Precise Determination of ^{6}Li Cold Collision Parameters by Radio-Frequency Spectroscopy on Weakly Bound Molecules. *Physical review letters*, **94**(10):103201, 2005.

[53] C. Sanner, E.J. Su, A. Keshet, R. Gommers, Y. Shin, W. Huang, and W. Ketterle. Suppression of Density Fluctuations in a Quantum Degenerate Fermi Gas. *arXiv:1005.1309v3 [cond-mat.quant-gas]*, 2010.

[54] JP Gaebler, JT Stewart, TE Drake, DS Jin, A. Perali, P. Pieri, and GC Strinati. Observation of pseudogap behavior in a strongly interacting Fermi gas. *arXiv:1003.1147v1 [cond-mat.quant-gas]*, 2010.

[55] S. Nascimbene, N. Navon, KJ Jiang, L. Tarruell, M. Teichmann, J. Mckeever, F. Chevy, and C. Salomon. Collective oscillations of an imbalanced Fermi gas: axial compression modes and polaron effective mass. *Physical review letters*, **103**(17):170402, 2009.

[56] A. Schirotzek, C.H. Wu, A. Sommer, and M.W. Zwierlein. Observation of Fermi polarons in a tunable Fermi liquid of ultracold atoms. *Physical review letters*, **102**(23):230402, 2009.

[57] S. Tan. Large momentum part of fermions with large scattering length. *arXiv preprint cond-mat/0508320*, 2005.

[58] S. Tan. Energetics of a strongly correlated Fermi gas. *Annals of Physics*, **323**(12):2952–2970, 2008.

[59] S. Tan. Generalized virial theorem and pressure relation for a strongly correlated Fermi gas. *Annals of Physics*, **323**(12):2987–2990, 2008.

[60] JT Stewart, JP Gaebler, TE Drake, and DS Jin. Verification of universal relations in a strongly interacting Fermi gas. *arXiv:1002.1987v1 [cond-mat.quant-gas]*, 2010.

Danksagung

An dieser Stelle möchte ich mich gerne bei allen Personen bedanken, die zum Gelingen dieser Arbeit beigetragen haben:

Prof. Markus Oberthaler danke ich dafür, dass er mir die Möglichkeit gegeben hat in seiner Gruppe zu arbeiten und direkt am NaLi-Experiment involviert zu sein. Seine offene Art und positives Feedback ermöglichten eine angenehme Arbeitsatmosphäre.

Bei Prof. Selim Jochim bedanke ich mich für die Zweitkorrektur dieser Arbeit.

Mein Dank gilt dem gesamten NaLi-Team, das für eine angenehme Arbeitsatmosphäre im Labor gesorgt und mit dem man auch außerhalb des Labors zum Beispiel bei gelegentlichen Grillabenden sehr gut die Zeit verbringen konnte. Insbesondere gilt mein Dank:

- Tobias Schuster, der mich exzellent bei dieser Arbeit betreut und sie auch korrekturgelesen hat. Trotz seiner Doppelbelastung (er betreute parallel auch Andrea) nahm er sich immer die Zeit meine Fragen im Detail zu beantworten, im Notfall auch ein zweites Mal. Ich habe wirklich eine Menge von ihm lernen können und seine unkomplizierte Art machte die Arbeit im Labor sehr kurzweilig und angenehm. Nebenbei färbte auch seine Begeisterung fürs Mountainbiken etwas auf mich ab (die für den 1. FC Kaiserslautern glücklicherweise nicht), was aber nichts daran geändert hat, dass er mich am Königstuhl immer noch gnadenlos abzieht. Ich hätte mir wirklich keinen besseren Betreuer für diese Arbeit wünschen können.

- Steven Knoop, unserem Postdoc, der sich immer die Zeit nahm mir das Experiment im Detail zu erklären und der uns auch bei den Imaging Sequenzen geholfen hat. Außerdem stellte er des öfteren seinen Balkon zum gemeinsamen Grillen zur Verfügung und er erklärte mir während der Weltmeisterschaft die niederländische Fußballseele. Ich hoffe immer noch auf ein Finale Niederlande gegen Deutschland.

- Raphael Scelle, der immer ein offenes Ohr für Fragen hatte, insbesondere wenn ich auf der Suche nach den richtigen MatLab-Befehlen war und mit dem die Arbeit im Labor stets spaßig war ('Brillen auf!'). Am Ende half er auch beim Korrekturlesen meiner Arbeit als Tobias schon in Les Huches war.

- Jens Appmeier, der mir meine Fragen immer ausführlich beantwortet hat. Da er gerade seine Doktorarbeit beendete als ich mit Schreiben anfing, überließ er mir dankenswerterweise auch seinen Arbeitsplatz im Büro.

- Andrea Bergschneider, ebenfalls Bachelor Studentin am NaLi, mit der das Arbeiten sehr angenehm war und die verhinderte dass beim Schreiben dieser Arbeit Frust aufkam, denn geteiltes Leid ist bekanntlich halbes Leid.

- Arno Trautmann, dem neuen Diplomanden am Experiment, der mich mitunter an seiner Latex Weisheit teilhaben ließ.

Dem NaLi-Team wünsche ich deshalb für die nahe Zukunft viel Erfolg und: *May the Force be with you!*

Des Weiteren möchte ich mich bei den (positiv) Verrückten von *Matterwave Stützrad* bedanken, die mich allwöchentlich den Königstuhl oder den weißen Stein mit dem Mountainbike hinaufgetrieben haben und ohne die ich mich wohl kaum dazu motiviert hätte (das ganze fand wohlgemerkt um 7.30 Uhr morgens statt). In der Zwischenzeit habe ich nun auch Radwege kennengelernt, die wohl nur mit einem GPS Gerät auffindbar sind.

Den Mitgliedern der anderen Arbeitsgruppen – ATTA, BEC, BECK und AEgIS – danke ich für die angenehme Gruppenatmosphäre, die Hilfsbereitschaft wenn man mal auf der Suche nach Laborequipment war und die mitunter interessanten Gesprächsthemen bei der wöchentlichen Frühstücksrunde.

Bei Jürgen Schölles von der Elektronik-Abteilung bedanke ich mich, der die Loop Amplifier unseren Bedürfnissen angepasst und der mir auch schon bei meinem vorherigen Projektpraktikum bei elektronischen Problemen geholfen hat.

Und zu guter letzt möchte ich noch die *Choco Bistro Doppelkekse* (eine billigere Kopie der Prinzenrolle) erwähnen, die einen festen Platz in unserem Büro haben und somit das Experiment am Leben erhalten. Auch für die Bachelorarbeit waren sie als Frühstücks- sowie Abendessenersatz oder einfach nur gegen aufkommenden Frust stets im Einsatz.

Erklärung

Ich versichere, dass ich diese Arbeit selbstständig verfasst und keine anderen als die angegebenen Quellen und Hilfsmittel benutzt habe.

Heidelberg, den 06.07.2010

....
(Unterschrift)